nature medicine

ARTICLES

https://doi.org/10.1038/s41591-020-0882-8

Check for updates

Chemotherapy-induced ileal crypt apoptosis and the ileal microbiome shape immunosurveillance and prognosis of proximal colon cancer

Maria Paula Roberti[1,2,3], Satoru Yonekura[1,2,4], Connie P. M. Duong[1,2], Marion Picard[1,2,5], Gladys Ferrere[1,2], Maryam Tidjani Alou[1,2], Conrad Rauber[1,2,4], Valerio Iebba[1,2], Christian H. K. Lehmann[6], Lukas Amon[6], Diana Dudziak[6], Lisa Derosa[1,2,3], Bertrand Routy[1,2,4], Caroline Flament[1,2,3], Corentin Richard[7,8], Romain Daillère[1,2], Aurélie Fluckiger[1,2], Isabelle Van Seuningen[9], Mathias Chamaillard[10], Audrey Vincent[9], Stephanie Kourula[11,12], Paule Opolon[1], Pierre Ly[1,2], Eugénie Pizzato[1,2], Sonia Becharef[1,2], Juliette Paillet[4,13,14], Christophe Klein[13], Florence Marliot[15,16], Filippo Pietrantonio[17,18], Stéphane Benoist[19], Jean-Yves Scoazec[20], Peggy Dartigues[20], Antoine Hollebecque[21], David Malka[21], Franck Pagès[15,16], Jérôme Galon[15,16], Ivo Gomperts Boneca[5,22], Patricia Lepage[23], Bernard Ryffel[24], Didier Raoult[25], Alexander Eggermont[1,2,21], Tom Vanden Berghe[11,12], François Ghiringhelli[7,8], Peter Vandenabeele[11,12,26], Guido Kroemer[13,14,27,28,29] and Laurence Zitvogel[1,2,3,4,28] ✉

The prognosis of colon cancer (CC) is dictated by tumor-infiltrating lymphocytes, including follicular helper T (T_{FH}) cells and the efficacy of chemotherapy-induced immune responses. It remains unclear whether gut microbes contribute to the elicitation of T_{FH} cell-driven responses. Here, we show that the ileal microbiota dictates tolerogenic versus immunogenic cell death of ileal intestinal epithelial cells (IECs) and the accumulation of T_{FH} cells in patients with CC and mice. Suppression of IEC apoptosis led to compromised chemotherapy-induced immunosurveillance against CC in mice. Protective immune responses against CC were associated with residence of *Bacteroides fragilis* and Erysipelotrichaceae in the ileum. In the presence of these commensals, apoptotic ileal IECs elicited PD-1$^+$ T_{FH} cells in an interleukin-1R1- and interleukin-12-dependent manner. The ileal microbiome governed the efficacy of chemotherapy and PD-1 blockade in CC independently of microsatellite instability. These findings demonstrate that immunogenic ileal apoptosis contributes to the prognosis of chemotherapy-treated CC.

The intestinal mucosa is a dynamic interface between IECs, local immune cells and the microbial ecosystem[1]. Mucosal regulatory T cells suppress excessive inflammation but promote the earliest stages of immune-prone carcinogenesis via enhancement of interleukin (IL)-17 production at the expense of interferon-γ production[2]. Sustained gut microbial dysbiosis may be a risk factor for the exacerbation of colorectal inflammatory lesions, leading to overt carcinogenesis[3,4]. Variations in gut microbial

[1]Gustave Roussy Cancer Campus (GRCC), Villejuif, France. [2]Institut National de la Santé Et de la Recherche Médicale (INSERM) U1015, Equipe Labellisée—Ligue Nationale contre le Cancer, Villejuif, France. [3]Center of Clinical Investigations in Biotherapies of Cancer (CICBT) 1428, Villejuif, France. [4]Université Paris-Saclay, Le Kremlin-Bicêtre cedex, France. [5]Unit Biology and Genetics of the Bacterial Cell Wall, Institut Pasteur Paris, Paris, France. [6]Department of Dermatology, Laboratory of Dendritic Cell Biology, Medical Immunology Campus Erlangen, University Hospital of Erlangen, Friedrich-Alexander-University (FAU) of Erlangen-Nürnberg, Erlangen, Germany. [7]Department of Medical Oncology, Center GF Leclerc, Dijon, France. [8]Plateform Transfer in Biological Oncology, Dijon, France. [9]Inserm UMR-S 1172, Jean-Pierre Aubert Research Center, CHU Lille, University of Lille, Lille, France. [10]Laboratory of Cell Physiology, INSERM U1003, University of Lille, Lille, France. [11]Molecular Signaling and Cell Death Unit, VIB Inflammation Research Center, Ghent, Belgium. [12]Department of Biomedical Molecular Biology, Ghent University, Ghent, Belgium. [13]Equipe Labellisée par la Ligue Contre le Cancer, Université de Paris, Sorbonne Université, INSERM U1138, Centre de Recherche des Cordeliers, Paris, France. [14]Cell Biology and Metabolomics Platforms, Gustave Roussy Cancer Campus, Villejuif, France. [15]Laboratory of Integrative Cancer Immunology, INSERM U1138, Centre de Recherche des Cordeliers, Paris, France. [16]Service d'Immunologie Biologique, Hôpital Européen Georges Pompidou, Paris, France. [17]Medical Oncology Department, Fondazione IRCCS Istituto Nazionale dei Tumori, Milan, Italy. [18]Department of Oncology and Hemato-oncology, University of Milan, Milan, Italy. [19]Service de Chirurgie Digestive et Oncologique, Hôpital Bicêtre, Le Kremlin-Bicêtre, France. [20]Departement de Biologie et Pathologie Médicales, Gustave Roussy Cancer Campus, Villejuif, France. [21]Departement de Médicine Oncologique, Gustave Roussy Cancer Campus, Villejuif, France. [22]INSERM, Equipe Avenir, Paris, France. [23]Micalis Institute, INRA, AgroParisTech, Université Paris-Saclay, Jouy-en-Josas, France. [24]Molecular Immunology and Embryology, UMR 7355, CNRS, University of Orleans, Orléans, France. [25]Unité des Rickettsies, Faculté de Médecine, Université de la Méditerranée, Marseille, France. [26]Methusalem Program, Ghent University, Ghent, Belgium. [27]Pôle de Biologie, Hôpital Européen Georges Pompidou, Assistance Publique—Hôpitaux de, Paris, France. [28]Suzhou Institute for Systems Medicine, Chinese Academy of Medical Sciences, Suzhou, China. [29]Department of Women's and Children's Health, Karolinska University Hospital, Stockholm, Sweden. ✉e-mail: laurence.zitvogel@gustaveroussy.fr

communities during colorectal cancer (CRC) progression suggest a role for distinct bacterial species, including *Fusobacterium nucleatum*, enterotoxigenic *Bacteroides fragilis* and *Parvimonas micra*, in carcinogenesis[5–8].

The abundance, functional competence and spatial distribution of tumor-infiltrating T lymphocytes (TILs) within the tumor bed (also known as Immunoscore[9–11]) dictate the prognosis of CRC[10]. The chemokine CXCL13 and IL-21 are pivotal factors in the T_{FH}–B cell axis, correlating with survival of patients with CRC[12]. The tumor, immune and/or environmental cues that lead to accumulation of TILs in CRC remain to be elucidated. Previous studies have shown that lymphocyte infiltration is associated with microsatellite instability (MSI), resulting in the generation of truncated peptides produced by frameshift mutations[13–16]. Such neoantigens may predispose patients with MSI-high CRC to clinical benefit from immune checkpoint inhibitors (ICIs)[17]. Oxaliplatin (OXA) is the backbone of the chemotherapeutic regimen routinely used to treat patients with CC; it can induce immunogenic cell death (ICD) and elicit anticancer immune responses[9,18,19]. Surprisingly, combinations of OXA with ICIs have not so far proven superiority over OXA-based chemotherapy alone in advanced CRC[20]. Cytotoxicants not only target tumor cells but also affect dividing crypt-derived IECs, thereby perturbing the local microbiota[21]. Hence, studying the interplay between IECs, commensalism and immune cells during chemotherapy may reveal mechanistic features governing TIL function against CRC.

Here we show that the immunogenicity of OXA chemotherapy in proximal CC (pCC) relies on two biological features: (1) antigenicity provided by caspase-3/7-dependent apoptosis of crypt-derived IECs and (2) adjuvanticity of selected ileal bacterial families or species (Erysipelotrichaceae, *B. fragilis*). These features cooperate to elicit T_{FH} cell immune responses protective against tumor progression.

Results

Ileal apoptosis dictates the prognosis of colon cancer in mice and patients. Given the gastrointestinal side effects and mucosal cytotoxicity associated with chemotherapy in patients[22], we monitored ileal cell apoptosis by quantifying levels of cleaved caspase-3 (cCasp3) in healthy colon and ileal mucosae. These tissues were collected during right hemicolectomies in patients with pCC who had or had not received preoperative OXA-based chemotherapy (Extended Data Fig. 1a–c). Surprisingly, apoptosis was induced by chemotherapy only in the crypts of ilea, but not in the villi, lamina propria or healthy colons adjacent to tumors, in two independent cohorts (Supplementary Table 1, Fig. 1a,b and Extended Data Fig. 2a,b). Moreover, higher baseline levels of cCasp3 in ileal crypts (≥ median value) were associated with favorable prognosis in patients with stage IV pCC in univariate analyses (Fig. 1c), whereas Immunoscore was not, as previously reported[8]. Chemotherapy did not increase the overall abundance of TILs (Extended Data Fig. 2c) but enriched tumor beds with $CD4^+Bcl6^+$ T_{FH} cells in the discovery and validation cohorts (Fig. 1d), while reducing ileal lamina propria T_{FH} cells (Extended Data Fig. 2d). The density of tumoral $CD4^+Bcl6^+$ T_{FH} cells correlated with TILs and with ileal crypt apoptosis, but was negatively correlated with their residence in the ileal lamina propria (Extended Data Fig. 2e–g). The composition of distal (fecal) microbiota has been associated with CRC gene profiling[23] and distinguishes benign from malignant colon tumors[24]. We next analyzed changes in the ileal microbiota, collected in healthy ileal mucosae lining upstream from Bauhin's valve (Extended Data Fig. 1a) that were associated with ileal IEC apoptosis using 16S rRNA gene sequencing of 70 ileal mucus layers at the family and species taxonomic rank levels (Extended Data Fig. 1b). Ileal apoptosis correlated with the relative abundance of Erysipelotrichaceae, but negatively correlated with that of Fusobacteriaceae families (Fig. 1e). The overrepresentation of Fusobacteriaceae family members in the ilea was also negatively correlated with TIL abundance in pCC (Fig. 1f). A higher ileal relative abundance of *B. fragilis* (considering either tertiles or ventiles) selectively predicted long-term survival in these 70 patients, contrasting with other frequent *Bacteroides* spp. (such as *B. uniformis* and *B. caccae)* or Prevotellaceae family members that were associated with dismal prognosis in univariate analyses (Fig. 1g and Supplementary Tables 2–3). Interestingly, Bacteroidaceae and Erysipelotrichaceae resided in the same cluster and negatively correlated with Prevotellaceae in a nonsupervised hierarchical clustering of ileal taxonomic families (Supplementary Fig. 1). Hence, ileal apoptosis in patients with stage IV pCC is associated with significant variations of the local microbiome, as well as a redistribution of T_{FH} cells to the tumor bed that may influence clinical outcome.

To further investigate the mechanistic links between ileal apoptosis, microbiota and tumor immunosurveillance, we utilized the MC38 mouse model of MSI-high CC[25]. Pre-treatment with broad-spectrum antibiotics (ATB) (Supplementary Fig. 2a) reduced the efficacy of OXA against subcutaneous (s.c.) MC38 (Fig. 2a and Supplementary Fig. 2b) and prevented the release of antimicrobial peptides into feces (Extended Data Fig. 3a,b), suggesting a role for

Fig. 1 | Ileal apoptosis and microbiome dictate prognosis in stage IV pCC. a, Representative micrograph pictures of immunohistochemistry for cCasp3 in ileal and colonic paired specimens from patients with pCC without or after preoperative chemotherapy. Scale bar, 20 µm. Inset depicts a higher magnification field at the bottom of an ileal crypt; red arrows indicate cCasp3 staining. Scale bar, 5 µm. **b**, Statistical analysis of $cCasp3^+$ cells by automated quantification using an algorithm to select crypts. Nonprevious chemotherapy ileum $n=31$, colon $n=30$; previous chemotherapy ileum $n=14$, colon $n=14$ (validation cohort, patients described in Supplementary Table 1). Each dot represents one patient with pCC, box plot center lines correspond to the median value; lower and upper hinges correspond to the first and third quartiles (25th and 75th percentiles) and lower and upper whiskers extend from the box to 5th and 95th percentiles, respectively. Two-tailed Mann–Whitney *U*-test *P* value is shown. **c**, Kaplan–Meier survival curve of progression-free survival (PFS) and univariate two-sided log-rank analysis of patients with nontreated stage IV pCC from the validation cohort (ileum $n=18$, colon $n=13$) segregated in two subgroups according to the median value of $cCasp3^+$ cell density. **d**, Number of $CD4^+Bcl6^+$ double positive (T_{FH}) cells mm^{-2} assessed by immunohistochemical staining in tumors from patients with pCC without or after preoperative chemotherapy. Nonprevious chemotherapy discovery $n=33$, validation $n=37$; previous chemotherapy discovery $n=11$, validation $n=7$ (patients described in Supplementary Table 1). Box plot center lines correspond to the median value; lower and upper hinges correspond to the first and third quartiles (the 25th and 75th percentiles) and lower and upper whiskers extend from the box to 5th and 95th percentiles, respectively. Two-tailed Mann–Whitney *U*-test *P* value is shown. **e**, Correlations between $cCasp3^+$ density in ileal crypts and bacteria families in autologous ilea. Each dot represents one patient with pCC, $n=30$. Spearman's rank coefficients of correlation (r_s) and two-tailed *P* values are shown. The continuous and dotted lines show the regression line and 95% CIs, respectively. **f**, Heat map showing correlation coefficients between ileal bacteria families identified by 16S rRNA gene sequencing of ileal mucus and TIL density of $CD3^+$ and $CD8^+$ T cells in the invasive margin (IM) or the core of the tumor (CT) in $n=59$ paired samples of the discovery cohort. (Supplementary Tables 1 and Extended Data Fig. 1b). Spearman's rank coefficients of correlation (r_s) and two-tailed *P* values <0.05 (*) are depicted. **g**, Kaplan–Meier survival curves and univariate two-tailed log-rank analyses of $n=70$ patients with pCC (Supplementary Table 1), segregating the cohort according to tertiles of relative abundance of corresponding bacteria taxa (Supplementary Table 2).

gut microbiota in local and extra-intestinal effects of OXA. While OXA triggered apoptosis of both ileal and colonic IECs, there was significantly more apoptosis of the former ($P < 0.0003$), as described for patients with CC and only in the presence of an intact microbiome (Fig. 2b,c). Accordingly, baseline proliferation of ileal IECs, which significantly exceeded that of colonic IECs, was markedly affected by OXA therapy (Extended Data Fig. 3c,d).

To further study the impact of patient microbiota on the efficacy of OXA, we utilized an avatar model[26], in which the intestines of germ-free mice were colonized with human proximal colonic content (Extended Data Fig. 1a) from 12 patients with pCC (Supplementary Table 4). Two weeks later, these mice were inoculated with s.c. MC38 and another week later treated with OXA (Extended Data Fig. 3e). While the majority (8 of 12) of patient microbiota resulted in anti-tumor efficacy of OXA comparable or superior to that observed in mice reared in specific-pathogen-free (SPF) conditions (henceforth referred to as avatar responders (aRs)), four patients' microbiota induced complete resistance to this immunogenic chemotherapy

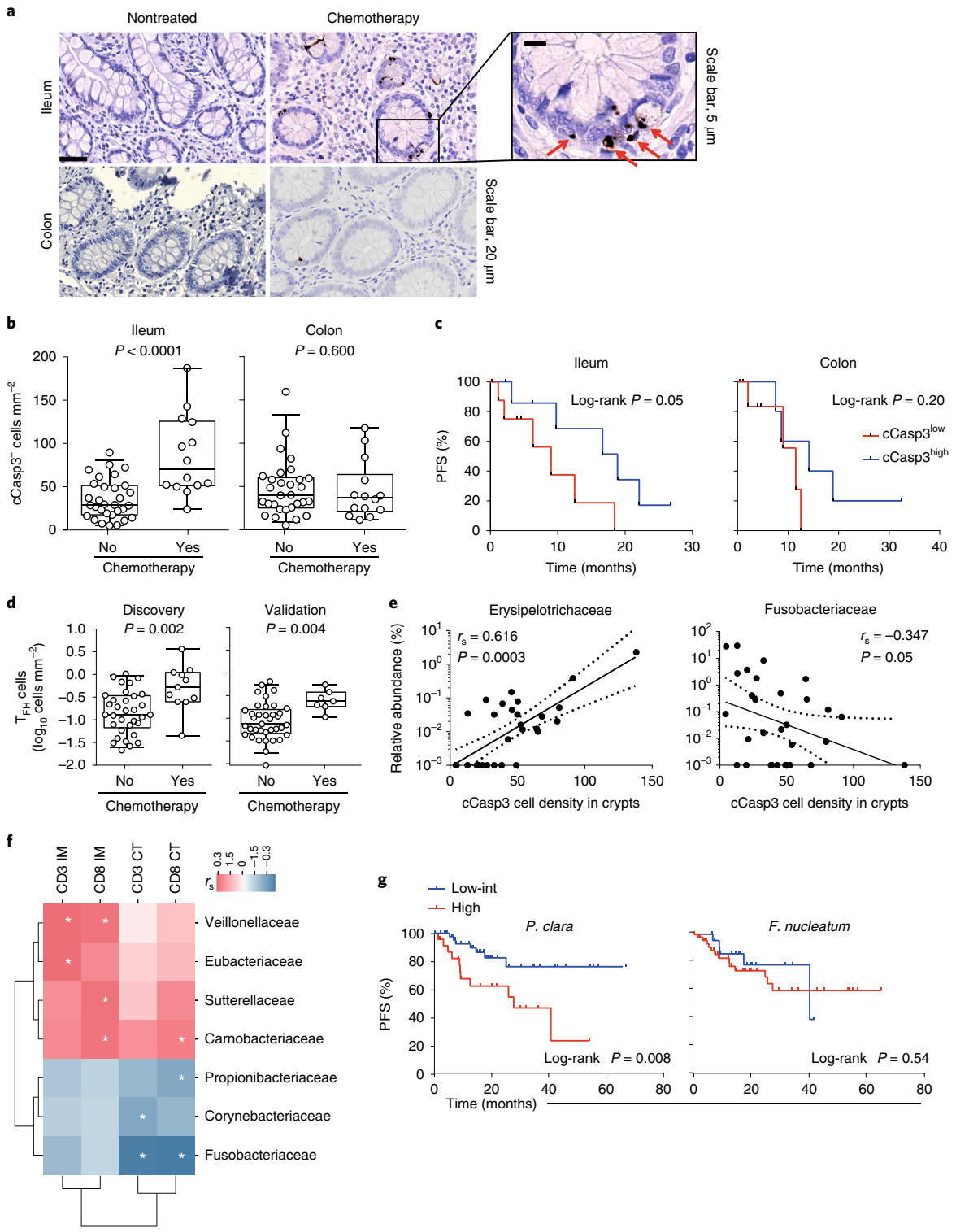

(avatar nonresponders (aNRs)) (Fig. 2d,e and Supplementary Fig. 2c). We performed 16S rRNA gene sequencing on the avatar feces and compared the mouse metagenomic profiles to that of the original patient sample (Supplementary Fig. 2d, illustrating the 12 clinically relevant families described in Fig. 1). The diversity of bacterial engraftment was driven by the host, with no significant differences among all recipients at family or species taxonomic rank levels (Supplementary Fig. 2e illustrates all species available in the dataset). However, supervised partial least squares discriminant analysis (PLS-DA) revealed that some species were differentially associated with aR versus aNR. In particular, *Paraprevotella clara* was strongly related to aNR status (Extended Data Fig. 3f and Supplementary Fig. 2f). Feces from avatar recipients (post-fecal microbiota transplant (FMT)) collected before starting OXA treatment also revealed increased colonization with *B. fragilis* in aR compared to aNR by quantitative PCR (Fig. 2h). We performed immunological phenotyping of T cell infiltrates in lymphoid organs, such as spleen and tumor draining lymph nodes (tdLNs), with the aim to dissect the interplay between regulatory T cells, IL-17-producing helper T cells (T_H17), cytotoxic T cell type 1 and T_{FH} cells as illustrated in our cohorts (Fig. 1) and as previously described[2]. There was a significant increase of ICOS-expressing $CXCR5^{hi}$ $PD\text{-}1^{hi}CD4^+$ T_{FH} cells in tdLNs of OXA-treated aR tumor bearers (Fig. 2f,g and Extended Data Fig. 3g) with a concomitant decrease of $CCR6^+CXCR3^-CD4^+$ T_H17-like cells (Extended Data Fig. 3h).

Consistently with patient data, MC38-bearing mice exhibited OXA-induced ileal apoptosis and their intestinal microbiome composition governed the T_{FH}/T_H17 balance in tdLNs.

Immunogenicity of caspase-3/7-dependent ileal apoptosis against colon cancer. We next sought to validate the relevance of ileal apoptosis for cancer immunosurveillance in other CC models. To do this, we immunized naive C57BL/6J or BALB/c mice using a syngeneic vaccine composed of primary (nonmalignant) ileal or colonic IECs collected from OXA- (or PBS)-treated syngeneic littermates, against a minimal tumorigenic dose (MTD) of MC38 or the microsatellite-stable (MSS) CC model CT26 (refs. [27,28]), respectively (Fig. 3a). We observed that ileal (and to a lesser extent colonic) IECs conferred partial protection against MC38 but not sarcoma nor cholangiocarcinoma in C57BL/6 mice, whereas ileal (and not colonic) IECs protected BALB/c mice against CT26 (but not breast cancers) (Fig. 3b–d, Extended Data Fig. 4a,b and Supplementary Fig. 3a). This vaccine conferred long-term protection with immunological memory lasting at least 12 weeks post-vaccination (Fig. 3e and Supplementary Fig. 3b). IECs from mice pre-treated in vivo with OXA were more efficient in reducing CC growth than untreated IECs (Fig. 3b,c). Only apoptotic IECs (annexin V^+) but not necrotic cells (obtained after freezing–thawing cycles) were immunogenic (Extended Data Fig. 4c,d and Supplementary Fig. 3c). Crypt- but not villi-derived dying IECs conveyed protection against MC38 (Extended Data Fig. 4e and Supplementary Fig. 3d). Of note, the mitotically active $Lgr5^+$ intestinal stem cells were dispensable for the immunogenicity of IECs (Extended Data Fig. 4f,g).

To analyze the differential immunogenicity of apoptosis versus necroptosis of ileal IECs, we collected OXA-exposed ileal mucosae from mice in which caspase-3/7 expression was ablated specifically in IECs ($Casp3/7^{\Delta IEC}$) or from *Ripk3*-deficient animals to vaccinate naive recipients. The immunizing potential of ileal IECs against MC38 cells was lost in the former (Fig. 3f) but not in the latter (Fig. 3g and Supplementary Fig. 3e) mice recipients, underscoring the role of apoptosis but not RIPK3-dependent necroptosis in the immunogenicity of ileal IECs. We next analyzed the impact of ileal IEC apoptosis in the tumor growth-reducing activity of OXA against day 7 established s.c. MC38 tumors. The antitumor efficacy and immunostimulatory capacity of OXA in $Casp3/7^{\Delta IEC}$ mice was significantly reduced compared to that in $Casp3/7^{fl/fl}$ littermate controls (Fig. 3h,i and Supplementary Fig. 3f).

Essential role for T_{FH} cells in the immunogenicity of ileal apoptosis. Given the accumulation of T_{FH} cells in tdLNs post-OXA in aR tumor bearers (Fig. 2g and Extended Data Fig. 3g,h) and in pCC from patients (Fig. 1d), we tested the effects of T cell depletion on the immunizing capacity of apoptotic ileal IECs. The vaccine efficacy relied on $CD4^+$ and $CD8^+$ T cells (Extended Data Fig. 5a) and elicited $CXCR5^{hi}PD\text{-}1^{hi}Bcl6^+$ cells expressing high levels of membrane ICOS in skin draining lymph nodes (dLNs) (Fig. 4a–c). These T_{FH} cells were also increased at day 7 post-OXA in the mesenteric lymph nodes (mLNs) of wild-type (WT) mice but not $Casp3/7^{\Delta IEC}$ mice, suggesting a crucial role for ileal apoptosis in the accumulation of T_{FH} cells (Fig. 4d). To evaluate the functional impact of T_{FH} cells on the immunogenicity of dying ileal IECs, we utilized four approaches. First, we observed that OXA-exposed ileal IECs exhibited a reduced immunizing capacity in a genetically T_{FH} cell-deficient

Fig. 2 | Impact of the microbiome in the efficacy of OXA in MC38 tumor bearers. a, Tumor size for OXA- and PBS-treated mice in water controls or under continuous ATB treatment. Each dot represents one mouse, the mean ± s.e.m. tumor size of five independent experiments is shown. Water PBS, $n=30$; water OXA, $n=30$; ATB PBS, $n=33$; ATB OXA, $n=30$. **b**,**c**. Representative micrographs (**b**) and statistical analysis (**c**) of automated quantification of positive staining of cCasp3 in paired healthy ilea and colons in MC38 s.c. tumor bearers untreated or treated with OXA (with or without concomitant ATB treatment) at 24 h. Mean ± s.e.m. is depicted. Water groups $n=20$ and ATB groups $n=5$. Scale bar, 50 µm. **d**, Avatar MC38 model system (experimental setting as in Extended Data Fig. 2e) using colon content from patients with pCC to colonize germ-free (GF) C57BL/6J recipients. Representative tumor growth curves for aR and aNR. Tumor size over time is represented as mean ± s.e.m. for natural tumor growth (PBS, $n=5$) or after OXA treatment ($n=4$) for one FMT. **e**, Box plots showing the percentage of decrease in tumor size per day of OXA treatment relative to the tumor size in corresponding PBS group for all aR and aNR tested (red and blue dots, respectively). Dotted line shows the SPF average response. Box plot center lines correspond to the median value; lower and upper hinges correspond to the first and third quartiles (the 25th and 75th percentiles); and lower and upper whiskers extend from the box to the smallest or largest value, correspondingly. aR1 PBS $n=5$, OXA $n=4$; aR2 PBS $n=4$, OXA $n=3$; aR3 PBS $n=5$, OXA $n=5$; aR4 PBS $n=5$, OXA $n=4$; aR5 PBS $n=6$, OXA $n=6$; aR6 PBS $n=7$, OXA $n=6$; aR7 PBS $n=5$, OXA $n=4$; aR8 PBS $n=5$, OXA $n=6$; aNR1 PBS $n=5$, OXA $n=4$; aNR2 PBS $n=7$, OXA $n=6$; aNR3 PBS $n=5$, OXA $n=4$; aNR4 PBS $n=6$, OXA $n=6$. Details of each FMT donor patient are shown in Supplementary Table 4. **f**, Heat map representation of flow cytometric analyses of T cell immunophenotyping in spleens and tdLNs as a means fold ratio between OXA- and PBS-treated groups at killing. Pooled data are from experiments shown in **e**. Spleen samples were: aNR PBS $n=23$, OXA $=19$; aR PBS $n=35$, OXA $=35$. tdLN samples were: aNR PBS $n=19$, OXA $n=20$; aR PBS $n=22$, OXA $n=30$. Only for $CXCR5^{hi}PD\text{-}1^{hi}/CD4^+$ and $CD19^+/CD45^+$ markers were: aNR PBS $n=19$, OXA $=22$; aR PBS $n=19$, OXA $=20$. **g**, T_{FH} cells in treated versus untreated aR versus aNR. Each dot represents one mouse aNR PBS $n=19$, OXA $=20$; aR PBS $n=19$, OXA $=22$. Mean ± s.e.m. is depicted. **h**, *B. fragilis*-specific qPCR determination of relative abundance of bacterium in fecal material collected at baseline (before treatment). Graph depicting pooled data from four aNR and eight aR in which *B. fragilis* was present (aNR $n=25$; aR $n=37$). Each dot represents one mouse. Mean ± s.e.m. is depicted. Statistics were mixed-effect modeling with specific software (Methods) for longitudinal tumor growth analysis (**e**,**d**) and Mann–Whitney *U*-test to compare two independent groups (after Kruskal–Wallis test was implemented for multiple groups) (**a**,**c**,**f**–**h**). Two-tailed *P* values are shown in the figures for **f**: $^*P<0.05$, $^{**}P<0.01$, $^{***}P<0.001$, $^{****}P<0.0001$.

mouse model, *Cxcr5*$^{-/-}$, compared to WT counterparts (Fig. 4e and Supplementary Fig. 4a). Second, neutralizing the CXCR5 ligand CXCL13 with specific antibodies negatively affected protection by this vaccine (Fig. 4f and Supplementary Fig. 4b). Finally, in conditional mutant *Bcl6*$^{fl/fl}$*Cre*^{CD4} in which T_{FH} cells were decreased >90% compared to controls[29], the OXA-exposed IEC vaccine no longer mediated long-term protection against an MTD challenge with s.c. MC38 and therapeutic OXA exhibited reduced capacity to induce accumulation of CXCR3^{+}CD4^{+} or CD8^{+} TILs (Supplementary Fig. 4c,d).

Given that T_{FH} cells are pivotal regulators of the germinal center responses and humoral immunity[30], we explored humoral immune responses and the impact of B cells on the immunizing potential of dying ileal IECs. Elevated serum levels of IgG2b were monitored 3 weeks post-immunization and this effect was blunted by CXCL13 neutralization and CD4^{+} T cell depletion (Fig. 4g and

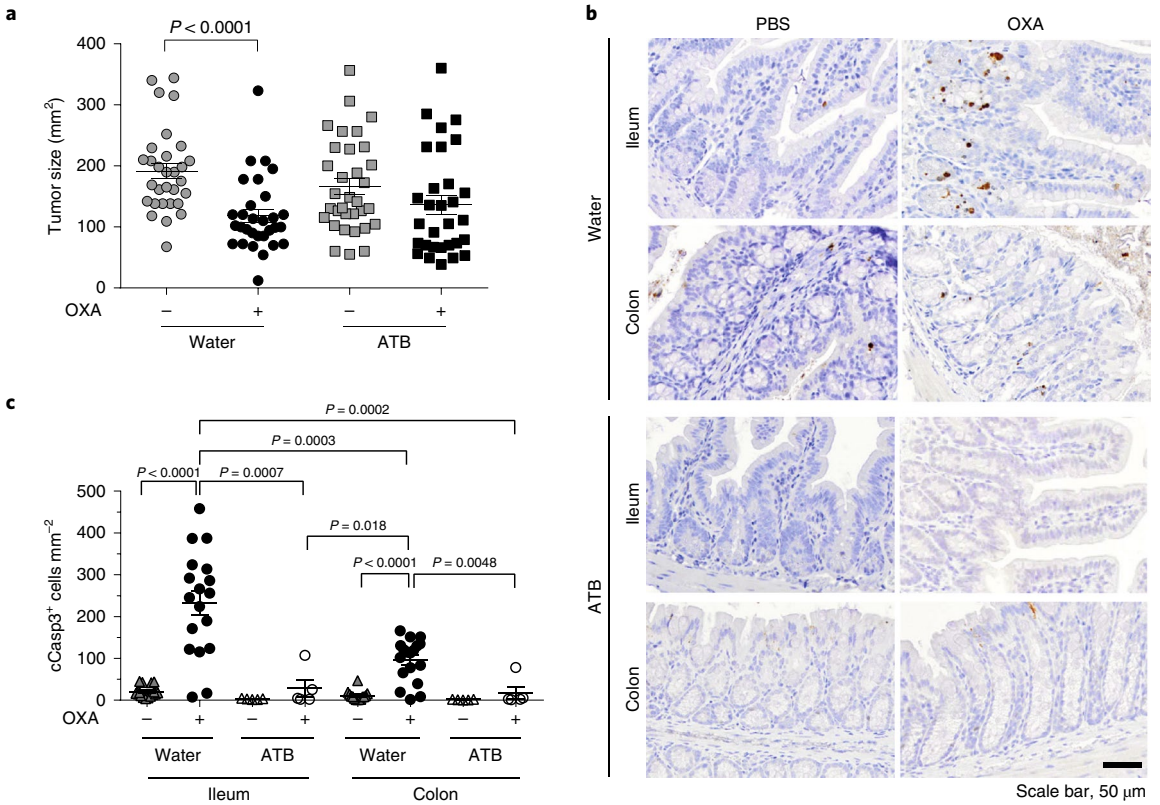

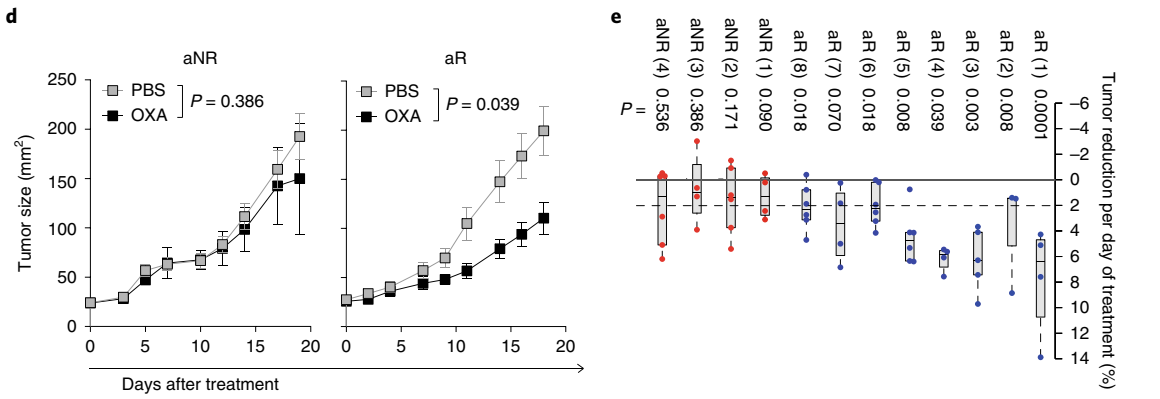

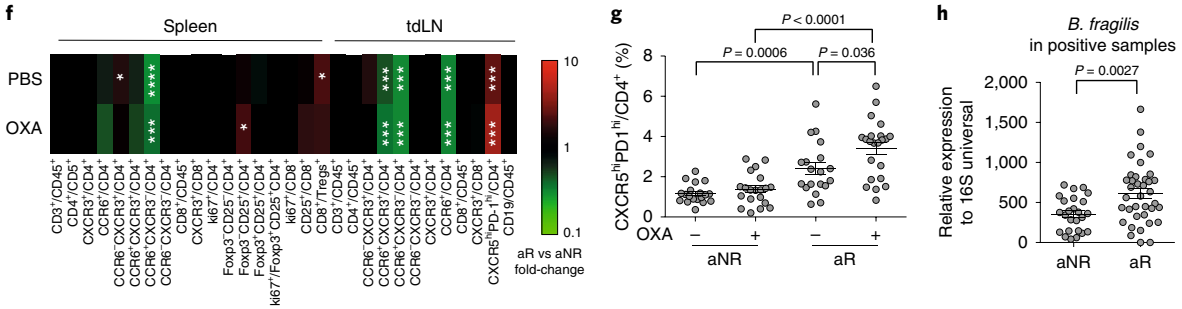

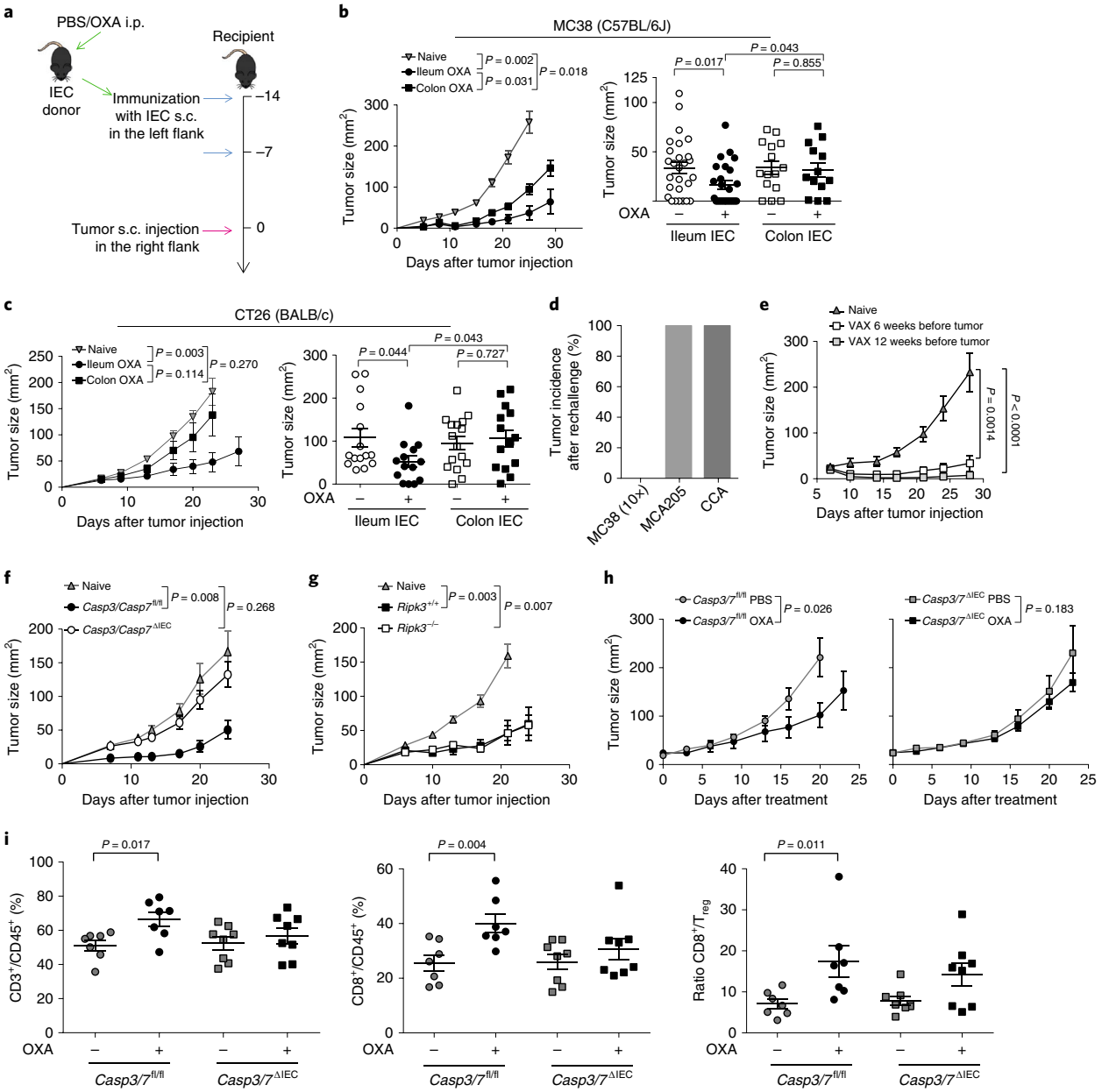

Fig. 3 | Protective role of intestinal caspase-3 and caspase-7 in the cell death of ileal IECs against CC. a, Experimental setting of vaccination with dying intestinal cells against CC. i.p., intraperitoneal. **b**, Vaccination of naive C57BL/6J mice using ileal or colonic IECs that were or were not exposed to OXA to protect against syngeneic transplantable CC, MC38. Tumor growth curves (left) showing one representative experiment (each group $n=5$, mean ± s.e.m. depicted) and tumor size at day 21 of 2–3 pooled experiments (right, 6–10 mice per group, ileum PBS $n=27$, ileum OXA $n=25$, colon PBS n = 15, colon OXA $n=13$). Each data point represents one mouse, mean ± s.e.m. is depicted. **c**, Vaccination of naive BALB/c mice using ileal or colonic IECs that were or were not exposed to OXA to protect against syngeneic transplantable CC, CT26. Tumor growth curves (left, naive $n=6$, ileum OXA $n=8$, colon OXA $n=8$, mean ± s.e.m. is depicted) showing one representative experiment and tumor size at day 21 of 2–3 pooled experiments (right, 6–10 mice per group ileum PBS $n=15$, ileum OXA $n=14$, colon PBS $n=16$, colon OXA $n=14$). Each data point represents one mouse, mean ± s.e.m. is depicted. **d**,**e**, Long-term protective antitumor immunity using ileal IEC-based immunization. Tumor rechallenge at day 14 (**d**) after complete tumor rejection in **a**–**c** settings using ten times the MTD of autologous MC38 versus the MTD of irrelevant syngeneic cancer cells (MCA205 and CCA) or at week 12 post-immunization (**e**). VAX, vaccinated groups. Percentages of tumor-bearing mice post-implantation of various malignancies (**d**). $n=6$ mice per group in three independent experiments for each cell line. For tumor growth kinetics (**e**), mean ± s.e.m. is depicted. $n=6$ and 10 mice per group for naive and vaccinated groups, respectively. **f**,**g**, Vaccination experiment using WT littermates or genetic variants, *Casp3/7*$^{\Delta IEC}$ (**f**) or *Ripk3*$^{\Delta IEC}$ (**g**), as ileal IEC donors to immunize WT hosts. Mean ± s.e.m. is depicted, $n=6$ mice/group showing one representative experiment out of two independent experiments yielding similar results. **h**, Tumor growth kinetics of MC38 treated or not treated with OXA at 7 d post-implantation in *Casp3/7*$^{\Delta IEC}$ mice compared to *Casp3/7*$^{fl/fl}$. One representative experiment out of two independent experiments yielding similar results is shown. *Casp3/7*$^{fl/fl}$ PBS $n=5$, *Casp3/7*$^{fl/fl}$ OXA $n=5$, *Casp3/7*$^{\Delta IEC}$ PBS $n=6$, *Casp3/7*$^{\Delta IEC}$ $n=7$. Mean ± s.e.m. is depicted. **i**, Flow cytometric analyses of various T cell subsets CD3$^+$, CD8$^+$ and CD8/CD4$^+$Foxp3$^+$ ratios at 10 d post-OXA. One representative experiment out of two yielding similar results is shown. *Casp3/7*$^{fl/fl}$ PBS $n=7$, *Casp3/7*$^{fl/fl}$ OXA $n=7$, *Casp3/7*$^{\Delta IEC}$ PBS $n=7$, *Casp3/7*$^{\Delta IEC}$ $n=8$. Each data point represents one mouse, mean ± s.e.m. is depicted. Statistics used were mixed-effect modeling with a specific software (Methods) for longitudinal tumor growth analysis (**b** left, **c** left, **e**–**h**) and Mann–Whitney *U*-test for comparison of two independent groups (after Kruskal–Wallis test was implemented for multiple groups) (**b** right, **c** right, **i**). Two-tailed *P* values are shown in figures.

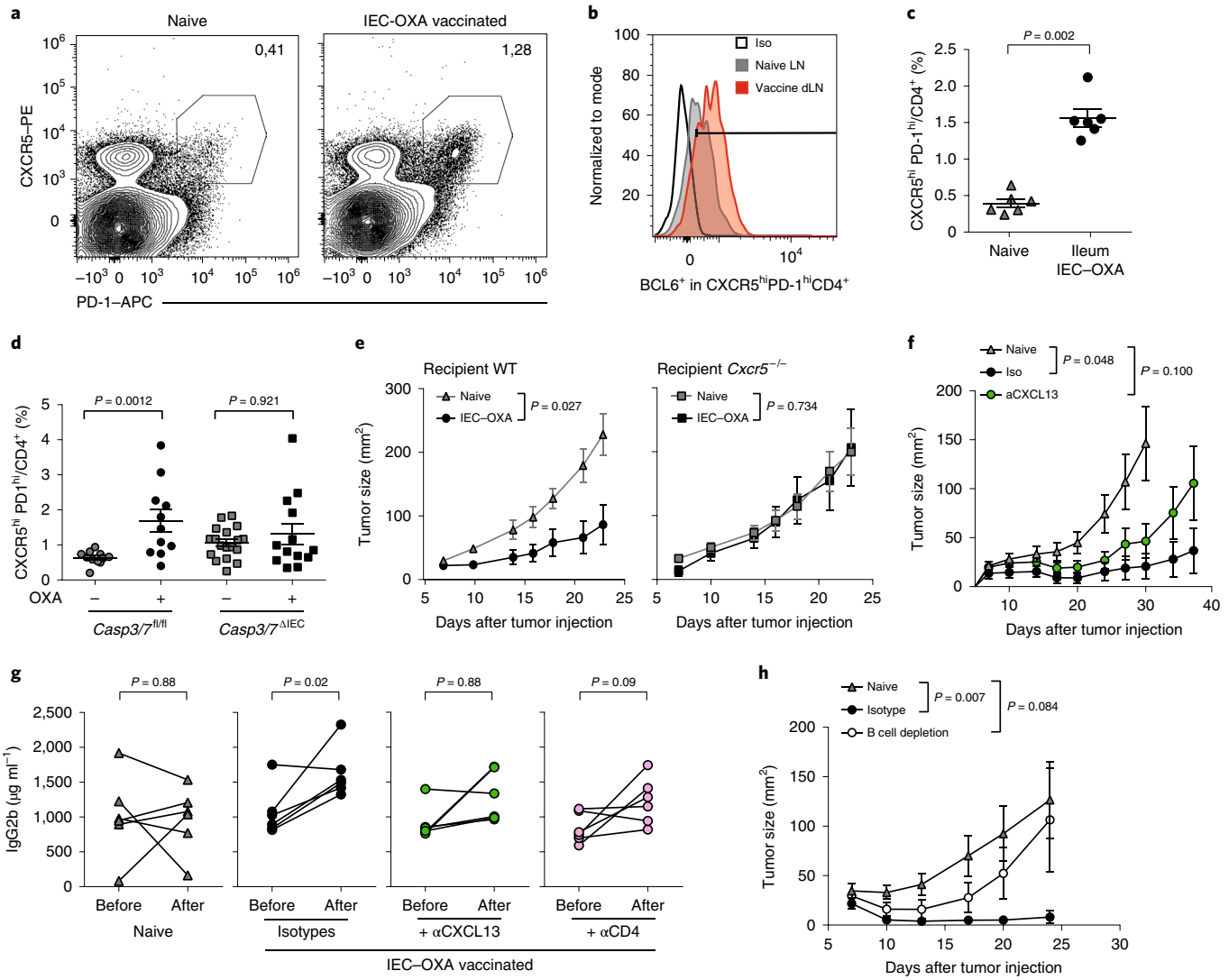

Fig. 4 | Mandatory role of T_{FH} cells in the immunogenicity of dying ileal IECs. a,**b**, Representative flow cytometry dot plot depicting percentages of T_{FH} cells (defined as CXCR5^{hi}PD-1^{hi}CD4^{+} cells in the viable CD3^{+}CD45^{+} population) from dLNs (**a**) and overlay of mean fluorescence intensities of Bcl6 expression in the CXCR5^{hi}PD-1^{hi}CD4^{+} population (**b**). Black line histogram corresponds to staining with the isotype control Ab. One experiment was performed. **c**, Flow cytometry analyses of percentages of T_{FH} cells in vaccinated dLNs defined as defined in **a**,**b** 7 d after the second immunization. Each data point represents one mouse, mean ± s.e.m. is depicted, $n = 6$ mice/group. **d**, Flow cytometry analysis of percentages of T_{FH} cells as defined in **a**,**b** in mLNs of tumor bearers from the indicated genetic background treated or not with OXA and killed at day 21. Pooled data are from two independent experiments. *Casp3/7*$^{fl/fl}$ PBS $n = 11$, *Casp3/7*$^{fl/fl}$ OXA $n = 11$, *Casp3/7*$^{\Delta IEC}$ PBS $n = 18$, *Casp3/7*$^{\Delta IEC}$ $n = 13$. Each dot represents one mouse mLN. Mean ± s.e.m. is depicted. **e**,**f**, Dying (OXA-exposed) ileal IEC vaccination as in Fig. 3a. in WT C57BL/6 mice or littermates harboring *Cxcr5* genetic defects (**e**) or co-treated with neutralizing anti-CXCL13 (**f**) or isotype control Ab. After vaccination, mice were challenged with the MTD of MC38 2–3 weeks later. Tumor growth kinetics are depicted as mean ± s.e.m., $n = 6$ mice/group. **g**, ELISA monitoring of serum levels of IgG2b at 4 weeks at mice killing, each dot representing one mouse in the experiment of s.c. vaccination using OXA-exposed ileal IECs in the presence of depleting or neutralizing antibodies (anti-CD4, anti-CXCL13 or isotype control Abs). A representative experiment out of two is depicted, comprising $n = 6$ mice/group. Two-sided Wilcoxon signed-rank test. **h**, Vaccination experiment as in **f** but using B cell-depleting Abs. Tumor growth kinetics are depicted in a representative experiment. Statistics, unless otherwise specified, were mixed-effect modeling with a specific software (Methods) for longitudinal tumor growth analysis (**e**,**f**,**h**) and Mann–Whitney *U*-test to compare two independent groups (after a Kruskal–Wallis test was implemented for multiple groups) (**c**,**d**). Two-tailed *P* values are shown in the figures.

Extended Data Fig. 5a). Systemic B cell depletion compromised the prophylactic antitumor effects of OXA-exposed ileal IECs (Fig. 4h and Supplementary Fig. 4e).

We conclude that OXA-induced apoptotic cell death of ileal IECs stimulates a T_{FH} cell response that contributes to the efficacy against CC of the prophylactic vaccine and chemotherapy in avatar mice and correlates with favorable Immunoscores in patients with pCC.

Mechanisms underlying the priming of T_{FH} cells with oxaliplatin. Intrigued by the impact of the microbiome in avatar mice (Fig. 2e) and the deleterious effect of ATB on OXA-mediated ileal IEC apoptosis and tumor growth reduction (Fig. 2a–c), we suspected that the ileal microbiome might contribute to the adjuvanticity of the IEC vaccine against CC. In support of this hypothesis, the immunogenicity of OXA-treated ileal IECs collected from SPF mice was superior to that of IECs from germ-free mice (Fig. 5a

and Supplementary Fig. 5a). We next tested the relevance of various damage- or microbe-associated molecular patterns released from OXA-exposed ileal IECs for the adjuvanticity of apoptosis. We immunized naive WT C57BL/6J mice with OXA-treated ileal IECs derived from *Entpd1*, Tlr2/Tlr4, Tlr9, Il1αβ or *Il18*-deficient syngeneic mice or OXA-exposed ileal WT IECs in which damage-associated molecular patterns that are usually associated with ICD (ATP, calreticulin and HMGB1) were neutralized by antibodies or pharmacological blockers. The immunogenicity of WT ileal IECs was significantly impaired when TLR2/4 (but not TLR9) or IL-1 (but not IL-18) were removed or when ATP release was inhibited or purinergic P2 receptors were blocked, yet did not depend on calreticulin nor on HMGB1 (Extended Data Fig. 5b,c). Reinforcing the role of specific microbes in the adjuvanticity of the CC vaccine, vaccination with ileal stem-cell-derived organoids (which are sterile) treated with OXA-accelerated MC38 progression compared to untreated organoids, suggesting that they were tolerogenic (Extended Data Fig. 6a and Supplementary Data Fig. 5b). Altogether, these findings indicate that ileal IECs exposed to conventional chemotherapy cannot induce a protective anticancer immune response in the absence of immunogenic microbiota.

To directly show that the ileal microbiota can restore the immunogenic properties of IECs, we supplemented initially sterile (and hence tolerogenic) OXA-treated ileal organoids with ten different microbiotas collected from the ileal mucosae of patients with pCC (Extended Data Fig. 6b and Supplementary Table 5). Only six of the ten ileal microbiotas were able to restore relative anticancer protection compared to several negative controls (such as naive nonimmunized mice, mice immunized with sterile OXA-treated organoids or mice immunized with ileal mucosae microbiota without organoids) (Fig. 5b, Extended Data Fig. 6c and Supplementary Fig. 5c). To identify the bacterial taxa that contribute to the immunogenicity of ileal IEC apoptosis, we used different and complementary technical approaches, namely, 16S rRNA gene sequencing and culturomics. By 16S rRNA gene sequencing, nonresponders (NRs) showed enrichment in the relative abundance of Prevotellaceae at the family taxonomic rank level (Extended data Fig. 6d) and of *Prevotella oralis*, *Alloprevotella rava*, *Prevotella clara*, *Paraprevotella xylaniphila* at the species taxonomic rank level (Extended Data Fig. 6e). Moreover, several other species belonging to the *Fusobacterium* genus (such as *F. canifelinum*, *F. periodonticum*, *F. nucleatum*) were significantly enriched in NRs compared to responder ileal microflora (Extended Data Fig. 6e). In parallel, the prevalence of distinct bacterial species in the ileal microbiota determined by culturomics, pointed to an increase in the abundance of live *Erysipeloclostridium ramosum* (among other species) in the responder microbiota (Extended Data Fig. 6f). These findings further illustrate the lack of immunogenicity of Prevotellaceae and Fusobacteriaceae already observed in the larger cohort of 70 ATB-naive patients with pCC for whom these taxa were negatively associated with ileal apoptosis, pCC Immunoscore and/or prognosis (Fig. 1e–g).

To further characterize the immune response elicited by dying ileal IECs during chemotherapy, we monitored the migration of dendritic cell (DC) subsets 24 h post-OXA. Migratory DCs (defined as $CD11c^{+}$ $MHC\text{-}I^{hi}$) composed mostly of $CD103^{+}CD11b^{-}$DC (conventional type 1 DCs, cDC1) accumulated in mLNs along with upregulation of IL-1β and IL-12 transcripts concomitantly to their depletion from the ileal (but not colonic) lamina propria (Extended Data Fig. 6g–i). Notably, the accumulation of T_{FH} cells in mLNs at 7 d after OXA administration was lost when cDC1 were absent in *Batf3* knockout mice or when the microbiota was perturbed by broad-spectrum ATB treatment (Fig. 5c).

Next, we analyzed the mechanism underlying the adjuvanticity of the ileal bacterial repertoire. Earlier reports demonstrated that recognition of viable bacteria by the innate immune system affected the ensuing T_H cell responses, in particular, the differentiation of T_{FH} cells. Sensing live bacteria can trigger the release of IL-1β and IL-12p70 by antigen-presenting cells and IL-1R1 signaling in T_{FH} cells[31,32]. Given that IL-1β featured in the cytokine fingerprint of mLNs following migration of ileal cDC1 to mLNs (Extended Data Fig. 6i) and that dying IECs collected from IL-1-deficient mice were unable to vaccinate against CC (Extended Data Fig. 5b), we performed immunohistochemistry to identify the main source of IL-1β in ileal and colonic mucosae 24 h after OXA injection. Mononuclear cells residing in the ileal (but not colonic) lamina propria were the unique source of IL-1β (Fig. 5d,e). Of note, IL-1R1 was indispensable for the immunogenicity of ileal apoptotic IECs because systemic administration of an IL-1R1 antagonist abrogated the effects of the vaccine and reduced the IgG2b-based humoral response associated with T_{FH} cells (Fig. 5f,g). Conversely, supplementation of the ileal stem-cell-derived organoids with recombinant IL-1β restored the immunogenicity of OXA-exposed sterile organoids (Fig. 5h) and boosted serum IgG levels (Extended Data Fig. 6j). Finally, neutralization of IL-12p40 or IL-12p70 drastically reduced the immunogenicity of dying ileal IECs to MC38 (Fig. 5i and Supplementary Fig. 5d), which is in accordance with the loss of IL-12p40 transcription in mLNs from *Batf3*-deficient mice (Extended Data Fig. 6k).

Fig. 5 | Role of Batf3 DC, IL-1R and IL-12 in the elicitation of T_{FH} cells during ileal cell death. a, Tumor growth kinetics (mean ± s.e.m.) of MC38 after vaccination with OXA-exposed ileal IECs from SPF versus GF mice. One representative experiment (with $n = 6$ mice/group) is depicted out of three, yielding similar results. **b**, Refer to the experimental setting in Extended Data Fig. 5b. Representative tumor growth curve in mice immunized with ileal mucosae-derived microbiota alone (left) and OXA–IECs plus ileal mucosae-derived microbiota (right) from the same patient conveying immunogenicity (five mice per group). Mean ± s.e.m. is depicted. **c**, Flow cytometry determination of $CXCR5^{hi}PD\text{-}1^{hi}CD4^{+}$ T lymphocytes from mLNs of MC38 tumor-bearing WT versus *Batf3* KO mice or WT animals treated with ATB (as in Fig. 2a), at day 7 post-OXA i.p. Two experiments were performed and each dot represents one mLN, $n = 5$ mice per group. Each data point represents one mouse, mean ± s.e.m. is depicted. **d**, Representative micrographs of immunohistochemical analyses of IL-1β of the lamina propria in paired ilea and colons from WT mice treated or not with OXA at 24 h. Scale bar, 50 µm. **e**, Statistical analysis of $IL\text{-}1\beta^{+}$ cells by automatic quantification. Samples size in ileum and colon were: water PBS $n = 5$, water OXA $n = 5$, ATB PBS $n = 4$, ATB OXA $n = 6$. Each data point represents one sample. Mean ± s.e.m. is depicted. **f**,**g**, Tumor sizes at killing (mean ± s.e.m.) of MC38 after vaccination with OXA-exposed ileal IECs from SPF mice treated or not with IL-1R1 antagonist (**f**) and concomitant monitoring of serum IgG2b levels by ELISA (**g**, two-sided Wilcoxon signed-rank test). Iso, isotype. Pooled data from two independent experiments are shown. Naive $n = 11$, IEC–OXA Iso $n = 12$, IEC–OXA αIL1R1 $n = 12$. Each data point represents one mouse. **h**, Tumor size at day 21 of MC38 after vaccination with OXA-exposed ileum crypt-stem-cell-derived organoids as donors to immunize WT hosts, with or without supplementation of rIL-1β. Pooled data are from two independent experiments. Naive $n = 11$, ctrl $n = 11$, rIL-1β $n = 10$. Each data point represents one mouse, mean ± s.e.m. is depicted. **i**, Tumor growth kinetics of MC38 after vaccination with OXA-exposed ileal IECs from SPF mice with isotype control or neutralizing anti-IL-12p40 or anti-IL-12p70 Abs. Pooled data are two independent experiments are shown. Naive $n = 12$, isotype $n = 12$, anti-IL-12p40 $n = 12$, anti-IL-12p70 $n = 6$. Each data point represents one mouse, mean ± s.e.m. is depicted. Statistics used unless otherwise specified, were mixed-effect modeling with a specific software (Methods) for longitudinal tumor growth analysis (**a**,**b**,**i**) and Mann–Whitney *U*-test used to compare two independent groups (after Kruskal–Wallis test was implemented for multiple groups) (**c**,**e**,**f**,**h**). Significant two-tailed *P* values are shown in the figures.

Altogether, the priming of T_{FH} cells is not only dictated by the executioner caspases 3/7 in ileal IECs but also by Batf3$^+$ cDC1 that produce IL-1β and IL-12 in mLNs, as well as the ileal microbiota that influences both caspase activation and cytokine production.

The adjuvanticity of ileal microbiota involved in the efficacy of PD-1 blockade. We screened a panel of live immunogenic or tolerogenic commensals isolated from ileal microbiotas of patients with pCC, identified by MiSeq 16S rRNA gene sequencing and culturomics (as described above in vaccine experiments, Extended

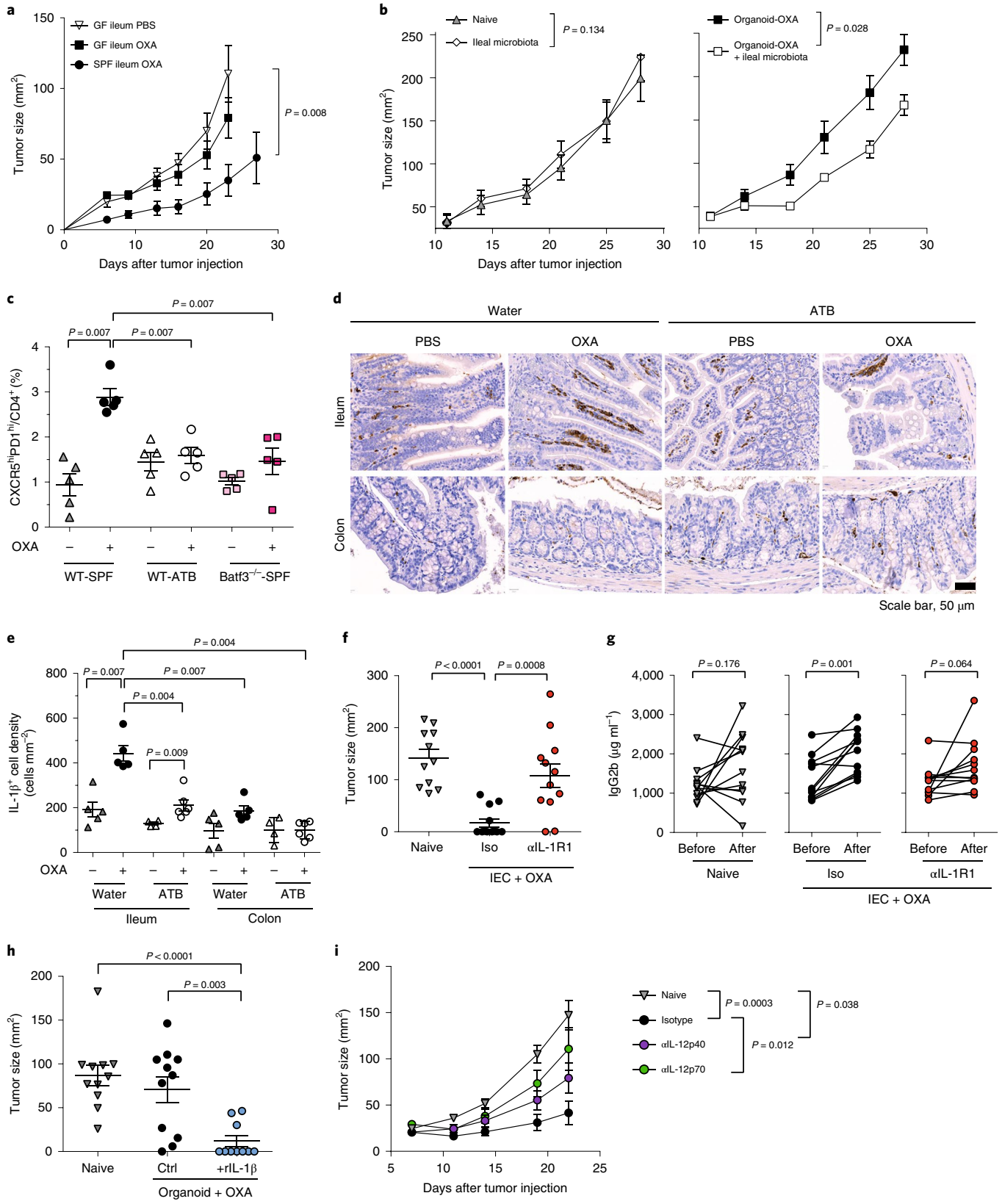

Data Fig. 6) or by virtue of their correlation with Immunoscore and survival of patients with pCC (Fig. 1), for their capacity to trigger the release of IL-1β and IL-12p70 by cDC1-like cells (generated from bone-marrow precursors in Flt3L-containing medium). We found that immunogenic bacteria (*B. fragilis*, a non-enterotoxigenic species, *E. ramosum* and *A. onderdonkii*) were superior to tolerogenic bacteria (*F. nucleatum*, *P. clara*, *B. uniformis* and *S. gallolyticus*) in stimulating IL-12p70 production by cDC1 (Extended Data Fig. 7a and Supplementary Fig. 6a). To evaluate immunological and tumor growth control-related relevance of the delicate equilibrium between immunogenic versus tolerogenic commensals residing in the ileum at the time of ileal IEC demise, we used three independent strategies. First, tolerogenic OXA-exposed organoids were admixed with different bacteria and evaluated for their capacity to reduce MC38 tumor growth (Fig. 6a). The immunogenic species *B. fragilis* enhanced vaccine efficacy, whereas the tolerogenic species *F. nucleatum* failed to do so (Fig. 6b), echoing similar results obtained with other immunogenic (*A. onderdonkii* and *E. ramosum*) or tolerogenic (*B. uniformis* and *S. gallolyticus*) commensals (Supplementary Fig. 6b). Second, we monocolonized germ-free C57BL/6J mice by oral gavage with immunogenic (*E. ramosum* or *A. onderdonkii*) versus tolerogenic (*S. gallolyticus*) bacteria, then collected OXA-treated ileal IECs to immunize naive SPF counterparts. Only immunogenic bacteria played an adjuvant role in these vaccines, protecting mice against MC38 (Supplementary Fig. 6c) and triggering IgG responses (Extended Data Fig. 7b) without inducing ileitis or colitis in vaccinated mice (Supplementary Fig. 6d,e). Third, given that human MSS pCC does not respond to PD-1 blockade in patients[17] and that PD-1^{hi}-expressing T_{FH} cells could be reinstated in their functional capacity by anti-PD-1 mAbs, we subjected mice bearing MSI (MC38) or MSS (CT26) tumors to gavage with immunogenic or tolerogenic commensals at the time of the combined chemoimmunotherapy with OXA and anti-PD-1 antibody (Ab) (Fig. 6c). This treatment was moderately additive against MC38 (MSI) and CT26 (MSS) in SPF mice (Supplementary Fig. 6f). However, *B. fragilis* or *E. ramosum* improved the effects of OXA + anti-PD-1 Ab, contrasting with *P. clara* or *F. nucleatum* that blunted the efficacy of the combination therapy (Fig. 6d,f). In parallel, immunogenic bacteria tended to increase serum IgG levels, whereas tolerogenic bacteria failed to do so (Fig. 6e and Extended Data Fig. 7c). Similar results were obtained in a humanized dysbiotic system by FMT (aNR1, Supplementary Table 4) in which the combination therapy, benefited from immunogenic but not tolerogenic bacteria (Fig. 6g). In the aforementioned settings, we confirmed adequate and comparable colonization of each of these exogenous commensals (Extended Data Fig. 7d). Of note, *F. nucleatum* failed to engraft in C57BL6/J mice, but could do so in BALB/c mice (Extended Data Fig. 7d).

These preclinical data highlight the regulatory role of the ileal microbiota in modulating the anticancer efficacy of immunogenic chemotherapy alone or combined with ICIs (Fig. 6h).

Discussion

Altogether, our findings suggest a role for the microbiota in governing the capacity of chemotherapy-induced ileal IEC apoptosis to elicit an antitumor immune response in patients with CC (scenario summarized in Fig. 6h). In this study, we purposely utilized an s.c. CC model to avoid any direct impact of the microbiota on the tumor, which allowed us to dissect the mechanistic interplay between the ileal microbiome and systemic immunomodulation. Ileal apoptosis in germ-free mice or in TLR2/4-deficient animals failed to elicit protective memory T cell responses against CC. Caspase-3/7-dependent apoptotic cell death of ileal IECs was sensed by CD103$^+$CD11b$^-$Batf3-dependent cDC1 only in the presence of immunogenic commensals, eliciting T_{FH} cell immune responses in mLNs dependent on IL-1R1 and IL-12. Activation of the executioner caspases in ileal crypts and the presence of immunogenic commensals conferred a favorable prognosis to patients with stage IV pCC.

Indeed, ileal IEC apoptosis facilitates the priming and activation of T_{FH} cells in the mLNs and their accumulation in tdLNs. In the absence of Bcl6$^+$CD4$^+$ T cells, CXCR5, CXCL13 or B cells, ileal apoptosis failed to contribute to OXA-induced anticancer immune responses and tumor growth reduction. Previous reports have supported the role of T_{FH} cells in human breast and CC immunosurveillance[12,33] and recent transcriptome analyses confirmed that T_{FH} cell metagenes are associated with a favorable clinical outcome[34]. The ileal microbiota is essential for the local activation of T_{FH} cells. Immunogenic commensals are distinguishable from tolerogenic bacteria in that they trigger both IL-1β and IL-12p70

Fig. 6 | Immunogenic ileal commensals boost the anticancer effects of immunotherapies against CC. a, Experimental setting of vaccination with organoids. Ileal stem-cell-derived organoids were exposed to distinct commensals and OXA ex vivo before s.c. injection to immunize naive mice against MC38. **b**, MC38 tumor sizes at killing from two independent experiments performed as indicated in the experimental setting in **a**, naive $n = 10$, *B. fragilis* $n = 16$, *F. nucleatum* $n = 15$. Each data point represents one mouse, mean ± s.e.m. is depicted. **c**–**f**, Experimental setting (**c**) of combinatorial therapeutic regimen against day 7 established MC38 (**d**) tumor-bearing mice reared in SPF conditions and supplemented with oral gavage (with various commensals) before i.p. administration of OXA. Tumor growth kinetics for each mouse are shown in a representative experiment out of two yielding similar results. Each group comprised $n = 6$ mice followed until killing of the control group. Detailed tumor growth kinetics in groups treated with OXA or anti-PD-1 alone or combination of both are presented in Supplementary Fig. 6f. **e**, ELISA monitoring of IgG responses in serum of mice treated as in **c** for MC38 in C57BL6J mice and in Extended Data Fig. 6c for CT26 in BALB/c mice. Two-sided Wilcoxon signed-rank test. **f**, As in **d** but with CT26 established tumors in BALB/c mice. **g**, As in **f** but combinatorial regimen was performed after FMT of one aNR patient (aNR1, Supplementary Table 4). Isotype $n = 5$, OXA + αPD-1 $n = 6$, OXA + αPD-1 + *B. fragilis* $n = 6$, OXA + αPD-1 + *F. nucleatum* $n = 6$. Each data point represents one mouse. **h**, Proposed model on the role of the ileal microbiome in regulating the balance between tolerance and immunity of dying IECs. Chemotherapeutic agents (such as OXA) act not only on the tumor cells but also on cycling ileal IECs of the crypts. Ileal crypt IECs undergo Casp3/7-dependent cell death, which is tolerogenic (does not induce T_{FH} nor B cell maturation, but instead promotes T_H17 accumulation in tdLNs) when the ileal microbiome is dominated by Fusobacteriaceae (such as *F. nucleatum*) or Prevotellaceae (such as *P. clara*) family members. Conversely, ileal crypt IECs undergo Casp3/7-dependent cell death which becomes immunogenic, inducing T_{FH} cell and B cell maturation with class-switched Ab IgG(2b) production and activation of (crypt/bacterium antigen-specific) CD8$^+$ T_c cell type 1 subsets, when the ileal microbiome is dominated by Erysipelotrichaceae family members (such as *E. ramosum*) or *B. fragilis*. Local immunity is triggered by the migration of lamina propria CD103$^+$CD11b$^-$(Batf3$^+$) DCs to the mLN where they elicit an IL-1β and IL-12-dependent T_{FH} cell immune response. PD-1^{hi} T_{FH} cells may respond to anti-PD-1 Ab in the setting of OXA-induced crypt cell death, paving the way to the additive/synergistic effects of the combinatorial regimen when immunogenic bacteria dominate the ileal microbiome. We surmise that T_{FH} cells play a helper role in effector functions of self-antigen reactive CD8$^+$ T cells or facilitate IgG-mediated antibody-dependent cellular cytotoxicity responses against cancer cells. Statistics used were, unless otherwise specified, mixed-effect modeling with a specific software (Methods) for longitudinal tumor growth analysis (**d**,**f**,**g**) and Mann–Whitney *U*-test used to compare two independent groups (after Kruskal–Wallis was implemented for multiple groups) (**b**). Significant two-tailed *P* values are shown in the figures.

release from migratory DCs, thereby increasing bacterial and/or self-antigen-specific T_{FH} cell or IgG2b responses. Moreover, the density of T_{FH} cells in patients with pCC correlated with ileal caspase-3 activation and TILs, suggesting that T_{FH} cells primed during ileal apoptosis may serve helper functions for antitumor effector/memory $CD8^+$ T cell responses recognizing (crypt-derived) self-antigens. Conversely, tolerogenic bacteria elicited the accumulation of $CD4^+$ T_H17 cells in tdLNs, a parameter that is associated with poor responses to OXA in avatar mice and in patients with pCC[35,36].

A variety of microbial structures can elicit T_{FH} cell responses. An innate signature of microbial viability, more specifically bacterial RNA, could trigger IL-1β-dependent differentiation of T_{FH} cells and germinal center B cells[31,37]. Activated $ICOS^+$ T_{FH} cells recirculate in the blood after mucosal vaccination with inactivated enterotoxigenic *Escherichia coli* and represent a biomarker of mucosal

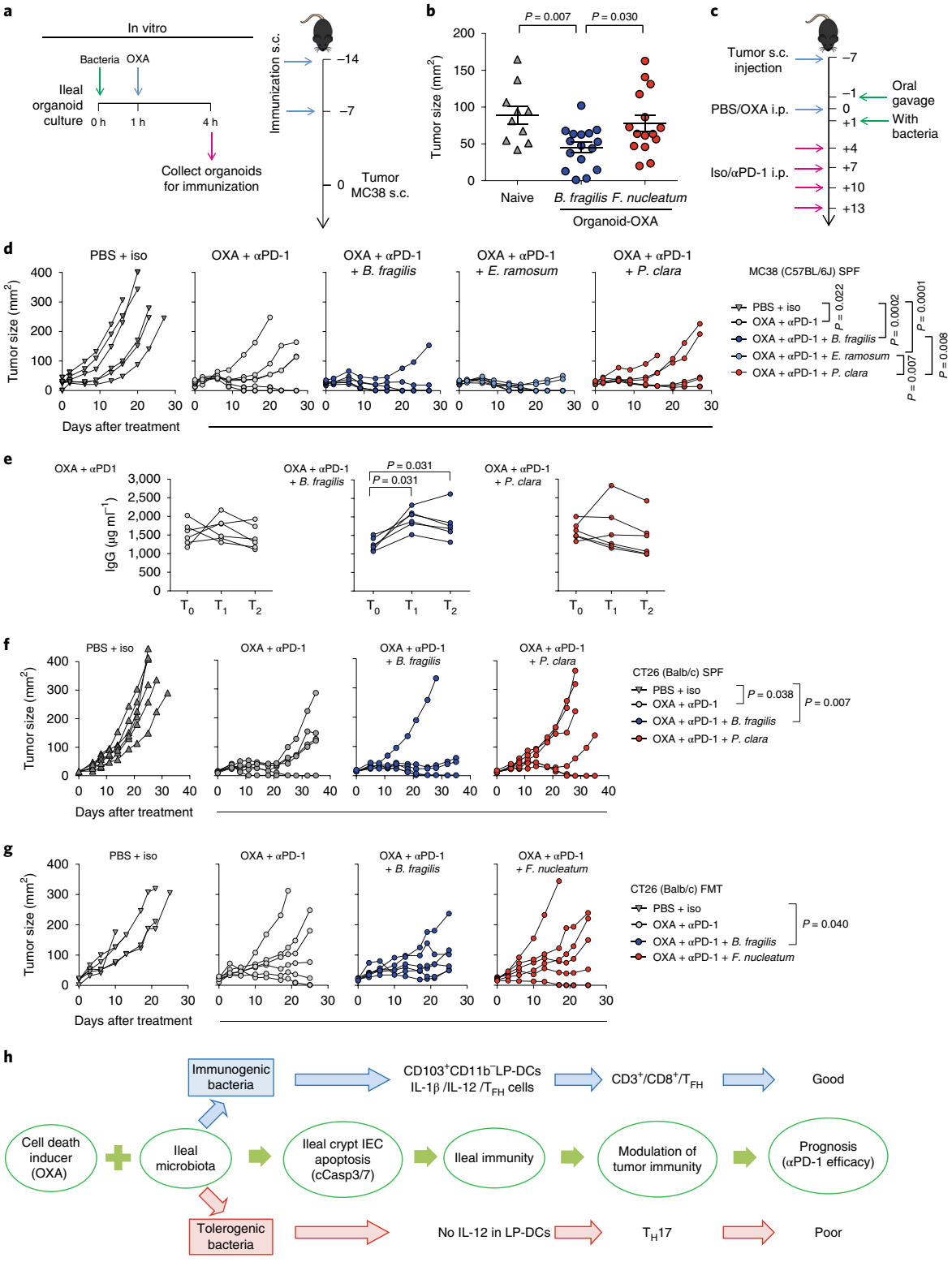

memory B cell responses in humans[38]. In line with these reports, our data show that ileal ICD depends on the microbiota and its capacity to trigger IL-1β-dependent T_{FH} cells. We, and others, have found that B cells are involved in tumor growth reduction subsequently to vaccination with dying ileal IECs or enforced tumor mutational burden[39], respectively. Moreover, successful combinatorial regimens and vaccination with apoptotic ileal cells increased IgG2b humoral responses. Nonetheless, the specificity of IgG responses (that may be directed against bacteria or tumor cells)[39–41] and the capacity of immunogenic commensals to invade tumor beds remain unclear and requires further in-depth exploration.

Our findings raise the theoretical possibility of OXA-induced self-reactive CD8+ T cell-dependent immunity that spares healthy tissues to specifically combat cancer, presumably due to the tightly controlled tolerance mechanisms in mucosal tissues[42,43]. This concept has been previously described by Ziegler and colleagues in spontaneous CRC, where elevated mitophagy (by genetic loss of *Stat3*) in IECs paved the way to adaptive anti-CC immunity[44].

Our study suggests potential new therapeutic avenues, including ileum IEC-targeted cell death inducers and bacterial adjuvants with the purpose of inducing immune responses against CC (self) antigens and of reinstating clinical responses to PD-1 blockade in MSS tumors. Ab–drug conjugates, such as those used to target cancer stem cells[45,46], may actually be able to reach these objectives.

Online content

Any methods, additional references, Nature Research reporting summaries, source data, extended data, supplementary information, acknowledgements, peer review information; details of author contributions and competing interests; and statements of data and code availability are available at https://doi.org/10.1038/s41591-020-0882-8.

Received: 28 August 2019; Accepted: 10 April 2020;
Published online: 25 May 2020

References

1. Sears, C. L. & Garrett, W. S. Microbes, microbiota, and colon cancer. *Cell Host Microbe* **15**, 317–328 (2014).
2. Geis, A. L. et al. Regulatory T cell response to enterotoxigenic *Bacteroides fragilis* colonization triggers IL-17-dependent colon carcinogenesis. *Cancer Discov.* **5**, 1098–1109 (2015).
3. Irrazábal, T., Belcheva, A., Girardin, S. E., Martin, A. & Philpott, D. J. The multifaceted role of the intestinal microbiota in colon cancer. *Mol. Cell* **54**, 309–320 (2014).
4. Belcheva, A. & Martin, A. Gut microbiota and colon cancer: the carbohydrate link. *Mol. Cell Oncol.* **2**, e969630 (2015).
5. Chen, W., Liu, F., Ling, Z., Tong, X. & Xiang, C. Human intestinal lumen and mucosa-associated microbiota in patients with colorectal cancer. *PloS ONE* **7**, e39743 (2012).
6. Geng, J., Fan, H., Tang, X., Zhai, H. & Zhang, Z. Diversified pattern of the human colorectal cancer microbiome. *Gut Pathog.* **5**, 2 (2013).
7. Nakatsu, G. et al. Gut mucosal microbiome across stages of colorectal carcinogenesis. *Nat. Commun.* **6**, 8727 (2015).
8. Saffarian, A. et al. Crypt- and mucosa-associated core microbiotas in humans and their alteration in colon cancer patients. *mBio* **10**, e01315 (2019).
9. Pagès, F. et al. Effector memory T cells, early metastasis, and survival in colorectal cancer. *N. Engl. J. Med.* **353**, 2654–2666 (2005).
10. Pagès, F. et al. International validation of the consensus Immunoscore for the classification of colon cancer: a prognostic and accuracy study. *Lancet* **391**, 2128–2139 (2018).
11. Mlecnik, B. et al. Histopathologic-based prognostic factors of colorectal cancers are associated with the state of the local immune reaction. *J. Clin. Oncol.* **29**, 610–618 (2011).
12. Bindea, G. et al. Spatiotemporal dynamics of intratumoral immune cells reveal the immune landscape in human cancer. *Immunity* **39**, 782–795 (2013).
13. Alexander, J. et al. Histopathological identification of colon cancer with microsatellite instability. *Am. J. Pathol.* **158**, 527–535 (2001).
14. Ogino, S. et al. Lymphocytic reaction to colorectal cancer is associated with longer survival, independent of lymph node count, microsatellite instability, and CpG island methylator phenotype. *Clin. Cancer Res.* **15**, 6412–6420 (2009).
15. Shia, J. et al. Value of histopathology in predicting microsatellite instability in hereditary nonpolyposis colorectal cancer and sporadic colorectal cancer. *Am. J. Surg. Pathol.* **27**, 1407–1417 (2003).
16. Tougeron, D. et al. Tumor-infiltrating lymphocytes in colorectal cancers with microsatellite instability are correlated with the number and spectrum of frameshift mutations. *Mod. Pathol.* **22**, 1186–1195 (2009).
17. Le, D. T. et al. PD-1 blockade in tumors with mismatch-repair deficiency. *N. Engl. J. Med.* **372**, 2509–2520 (2015).
18. Nosho, K. et al. Tumour-infiltrating T cell subsets, molecular changes in colorectal cancer, and prognosis: cohort study and literature review. *J. Pathol.* **222**, 350–366 (2010).
19. Salama, P. et al. Tumor-infiltrating FOXP3+ T regulatory cells show strong prognostic significance in colorectal cancer. *J. Clin. Oncol.* **27**, 186–192 (2009).
20. Shahda, S. et al. A phase II study of pembrolizumab in combination with mFOLFOX6 for patients with advanced colorectal cancer. *J. Clin. Oncol.* **35**, 3541–3541 (2017).
21. Nigro, G., Rossi, R., Commere, P.-H., Jay, P. & Sansonetti, P. J. The cytosolic bacterial peptidoglycan sensor Nod2 affords stem cell protection and links microbes to gut epithelial regeneration. *Cell Host Microbe* **15**, 792–798 (2014).
22. van Vliet, M. J., Harmsen, H. J. M., de Bont, E. S. J. M. & Tissing, W. J. E. The role of intestinal microbiota in the development and severity of chemotherapy-induced mucositis. *PLoS Pathog.* **6**, e1000879 (2010).
23. Purcell, R. V., Visnovska, M., Biggs, P. J., Schmeier, S. & Frizelle, F. A. Distinct gut microbiome patterns associate with consensus molecular subtypes of colorectal cancer. *Sci. Rep.* **7**, 11590 (2017).
24. Thomas, A. M. et al. Metagenomic analysis of colorectal cancer datasets identifies cross-cohort microbial diagnostic signatures and a link with choline degradation. *Nat. Med.* **25**, 667–678 (2019).
25. Yadav, M. et al. Predicting immunogenic tumour mutations by combining mass spectrometry and exome sequencing. *Nature* **515**, 572–576 (2014).
26. Routy, B. et al. The gut microbiota influences anticancer immunosurveillance and general health. *Nat. Rev. Clin. Oncol.* **15**, 382–396 (2018).
27. Castle, J. C. et al. Immunomic, genomic and transcriptomic characterization of CT26 colorectal carcinoma. *BMC Genomics* **15**, 190 (2014).
28. Germano, G. et al. Inactivation of DNA repair triggers neoantigen generation and impairs tumour growth. *Nature* **552**, 116–120 (2017).
29. Hollister, K. et al. Insights into the role of Bcl6 in follicular helper T cells using a new conditional mutant mouse model. *J. Immunol.* **191**, 2013 (1950).
30. Ueno, H., Banchereau, J. & Vinuesa, C. G. Pathophysiology of T follicular helper cells in humans and mice. *Nat. Immunol.* **16**, 142–152 (2015).
31. Barbet, G. et al. Sensing microbial viability through bacterial RNA augments T follicular helper cell and antibody responses. *Immunity* **48**, 584–598 (2018).
32. Ugolini, M. et al. Recognition of microbial viability via TLR8 drives TFH cell differentiation and vaccine responses. *Nat. Immunol.* **19**, 386–396 (2018).
33. Gu-Trantien, C. et al. CD4+ follicular helper T cell infiltration predicts breast cancer survival. *J. Clin. Invest.* **123**, 2873–2892 (2013).
34. Stoll, G., Pol, J., Soumelis, V., Zitvogel, L. & Kroemer, G. Impact of chemotactic factors and receptors on the cancer immune infiltrate: a bioinformatics study revealing homogeneity and heterogeneity among patient cohorts. *Oncoimmunology* **7**, e1484980 (2018).
35. Tosolini, M. et al. Clinical impact of different classes of infiltrating T cytotoxic and helper cells (T_h1, T_h2, T_{reg}, T_h17) in patients with colorectal cancer. *Cancer Res.* **71**, 1263–1271 (2011).
36. Lereclus, E. et al. A possible association of baseline serum IL-17A concentrations with progression-free survival of metastatic colorectal cancer patients treated with a bevacizumab-based regimen. *BMC Cancer* **17**, 220 (2017).
37. Pardi, N. et al. Nucleoside-modified mRNA vaccines induce potent T follicular helper and germinal center B cell responses. *J. Exp. Med.* **215**, 1571–1588 (2018).
38. Cárdeno, A., Magnusson, M. K., Quiding-Järbrink, M. & Lundgren, A. Activated T follicular helper-like cells are released into blood after oral vaccination and correlate with vaccine specific mucosal B cell memory. *Sci. Rep.* **8**, 2729 (2018).
39. Hollern, D. P. et al. B cells and T follicular helper cells mediate response to checkpoint inhibitors in high mutation burden mouse models of breast. *Cancer Cell* **179**, e21 (2019).
40. Luna Coronell, J. A. et al. The immunome of colon cancer: functional in silico analysis of antigenic proteins deduced from IgG microarray profiling. *Genomics Proteom. Bioinform.* **16**, 73–84 (2018).
41. Wang, H.-F. et al. Evaluation of antibody level against *Fusobacterium nucleatum* in the serological diagnosis of colorectal cancer. *Sci. Rep.* **6**, 33440 (2016).
42. Liu, Z. & Lefrançois, L. Intestinal epithelial antigen induces mucosal CD8+ T cell tolerance, activation, and inflammatory response. *J. Immunol.* **173**, 4324–4330 (2004).

43. Snook, A. E. et al. Lineage-specific T cell responses to cancer mucosa antigen oppose systemic metastases without mucosal inflammatory disease. *Cancer Res.* **69**, 3537–3544 (2009).
44. Ziegler, P. K. et al. Mitophagy in intestinal epithelial cells triggers adaptive immunity during tumorigenesis. *Cell* **174**, 88–101 (2018).
45. Junttila, M. R. et al. Targeting LGR5^{+} cells with an antibody-drug conjugate for the treatment of colon cancer. *Sci. Transl. Med.* **7**, 314 (2015).
46. Tao, Y. et al. Targeting of DDR1 with antibody-drug conjugates has antitumor effects in a mouse model of colon carcinoma. *Mol. Oncol.* **13**, 1855–1873 (2019).

Methods

Patient characteristics and clinical study details for discovery cohort. The inclusion criteria for the study were patients with colon adenocarcinoma who underwent right hemi-colectomy plus ileal resection (last 10 cm). Patients were not on ATBs at the moment of surgery. Three different health cancer centers participated in the study: Gustave Roussy Cancer Campus, Centre G-F Leclerc and Hôpital Bicêtre. Clinical studies were conducted according to the ethical guidelines and approval of the local ethics committee (CCPPRB). The study received the legal ethic authorization by the Ministère de l'Enseignement Supérieur et de la Recherche (AC-2013-1884). For feces collection, the study name was 'Oncobiotics', B2M ethics protocol number PP: 15-013. Written informed consent in accordance with the Declaration of Helsinki was obtained from all patients. Patient clinical characteristics are detailed in Supplementary Table 1.

Patient characteristics and clinical study details for validation cohort. The inclusion criteria for the study were patients with colon adenocarcinoma who underwent right hemi-colectomy plus ileal resection (last 10 cm). Samples were retrieved from formalin-fixed paraffin-embedded (FFPE) tissue from the pathology archives. Two different health centers participated in the study: Centre G-F Leclerc and Instituto Nazionale dei Tumori. Patient clinical characteristics are detailed in Supplementary Table 1.

Patient clinical categorization and follow-up. The information pertaining to tumor staging (TNM staging system of the American Joint Committee on Cancer) and MSI status was obtained in pathology reports. Information pertaining to cancer recurrence, death and causes of death was obtained from hospital records. All observations were censored at loss to follow-up and at the end of the study period. Overall survival was measured from the date of surgery to the date of death from any cause. PFS was measured from the date of surgery to the date of local or regional recurrence, distant metastases or death.

Preparation of patient samples for the study. Samples were collected at the time of surgery (Extended Data Fig. 1a,b). For samples of the luminal content from proximal colon, approximately 5 g of luminal content from the right colon were collected. Then 1 g of material was transferred into a sterile cryotube and immediately frozen at −80 °C for 16S rRNA gene sequencing. The remainder was suspended at 0.1 g ml^{-1} in brain–heart infusion (BHI) broth with 15% glycerol, homogenized and divided in 10-ml aliquots for FMT experiments. For samples of mucus adherent to the mucosae, after washing the surgical specimen, a noninvolved surface of the mucosae from the ileum and colon (distant from the tumor) was scraped using glass slides. Then 1 g of mucosal material was transferred into a sterile cryotube and immediately frozen at −80 °C for 16S rRNA gene sequencing. When possible, the remainder of the specimen was suspended at 0.1 g ml^{-1} in BHI broth with 15% glycerol. For samples of mucosal biopsies, approximately 4 cm^2 of ileal and nontumoral colonic tissue (distant from the tumor) that included at least the submucosa was removed and cut into small pieces (approximately 1 cm^2). All samples were FFPE after collection. Samples where technical analysis was performed are detailed in Extended Data Fig. 1b.

Tumor immune profiling by Immunoscore. Immune histological analysis of lymphocyte infiltration was performed on paraffin-embedded tumor samples. Two adjacent 4-µm sections were deposited on positively charged slides (SuperFrost+, Menzel Gläser). Immunoblots were performed using protocols optimized for the XT Benchmark (Ventana). Dewaxing and rehydration were carried out on the automaton as well as unmasking with Cell Conditioning 1 (Ventana) and EDTA buffer (pH 8). CD3 monoclonal Ab, clone 2GV6 (Ventana) was incubated for 20 min at 37 °C and the CD8 monoclonal Ab, clone C8/144B (DAKO) was incubated for 30 min at 37 °C. The ultraview DAB development system (Ventana) was used to visualize diaminobenzidine; counter-staining of the tissue was performed by incubating for 4 min with hematoxilin II (Ventana). Slides were scanned using the high-resolution slide scanner, NanoZoomer HT2.0 (Hamamatsu Photonics) at ×20 magnification with a resolution of 0.45 µm per pixel. Images of the scanned slides were imported into the Developer XD image analysis software (Definiens). Immune quantification of CD3$^+$ and CD8$^+$ was analyzed separately in the CT and IM.

Cell culture, reagents and tumor cell lines. MC38, MCA205 (syngeneic from C57BL/6J mice) and CT26 or 4T1 cell lines (syngeneic from BALB/c mice) were purchased from the American Type Culture Collection. The CCA cell line was a kind gift from G.J. Gores[47]. Cells were cultured in RPMI 1640 medium containing 10% FBS, 2 mM L-glutamine, 100 IU ml^{-1} penicillin/streptomycin, 1 mM sodium pyruvate and nonessential amino acids. All reagents were purchased from Gibco-Invitrogen. All cell lines were cultured at 37 °C with 5% CO_2 and regularly tested to be free of *Mycoplasma* contamination.

Mice. All animal experiments were carried out in compliance with French and European laws and regulations. The local institutional board (Ministère de la Recherche, de l'Ensiegnement Supérieur et de l'Innovation) approved all mouse experiments (permission numbers: 2014-071-1124 and 2017-020-8964). Female C57BL/6J and BALB/c mice were purchased from Harlan and Janvier, respectively. Mice were used between 7 and 14 weeks of age. GF C57BL/6J mice and *Il1ab*$^{-/-}$, *Il18*$^{-/-}$*Cd39/Entpd1*$^{-/-}$, *Tlr2/4*$^{-/-}$ and *Tlr9*$^{-/-}$ (all C57BL/6J genetic background) and WT littermates from the same breeding zones were obtained from the facility located at Cryopreservation, Distribution, Typage et Archivage. Lgr5-EGFP-IRES-creERT2 mice were used for lineage-tracing of Lgr5-expressing stem cells of the small intestine and were purchased from the Jackson Laboratory (JAX stock 008875)[48]. Homozygous *Cxcr5*-deficient mice, B6.129 S2(Cg)-Cxcr5^{tm1Lipp}/J, were a kind gift from R. Förster[49]. *Bcl6*$^{fl/fl}$*Cre*^{CD4} mice[29] were a kind gift from J.A. Harker (Imperial College London). *Batf3*-deficient mice, B6.129S(C)-Batf3^{tm1Kmm}/J, were obtained from the animal facility of University of Erlangen. In these mice, the first two exons of the transcription factor BatF3 have been removed inactivating this important transcription factor for cDC1 DCs[50]. Casp3$^{fl/fl}$; Casp7$^{fl/fl}$; Villin-Cre Tg (*Caspase3/Caspase7* IEC double knockout), RIPK3$^{-/-}$; Nnt$^{Mut/Mut}$ (*Rip3k* knockout) and respective WT littermate controls were obtained by P. Vandenabeele and some experiments were conducted in the animal facility of VIB-UGent Center for Inflammation Research. Caspase-3$^{fl/fl}$ and Caspase-7$^{fl/fl}$ mice were generated using ES clone HEPDO716_4_G05 and EPD0398_5_E02 (C57BL/6N), respectively from the International Mouse Phenotyping Consortium. The neomycin selection cassette was removed using FLPe deleter mice[51]. Intestinal specific targeting was achieved by crossing to Villin-Cre mice[52]. All other mouse experiments were performed at the animal facility in Gustave Roussy Cancer Campus, where animals were housed in SPF conditions or were maintained in isolators for GF and FMT experiments.

Antibiotic treatments. Mice were treated with an ATB solution containing ampicillin (1 mg ml^{-1}), streptomycin (5 mg ml^{-1}) and colistin (1 mg ml^{-1}) (Sigma-Aldrich), with or without the addition of vancomycin (0.25 mg ml^{-1}), which were added in the sterile drinking water of mice. Solutions and bottles were changed three times and once weekly, respectively. ATB activity was confirmed by analyzing feces for the presence of bacterial DNA by qPCR (see below) and by cultivating fecal pellets were resuspended in BHI broth + 15% glycerol at 0.1 g ml^{-1} on Columbia agar with 5% sheep blood plates for 48 h at 37 °C in aerobic and anaerobic conditions, weekly. The duration of ATB treatments was slightly different based on the experimental settings. In brief, to compromise the efficacy of OXA with ATB, mice were treated for 2 weeks before tumor implantation and continuously throughout the experiment.

Prophylactic and therapy setting in tumor models. *Subcutaneous model of MC38.* Syngeneic C57BL/6J mice were implanted with 1 × 10^6 MC38 WT cells s.c. and treated i.p. when tumors reached 20–30 mm^2 in size with 10 mg per kg OXA or vehicle (PBS). The composition of the commensal gut microbiota in the treated and nontreated groups was maintained and synchronized by cohousing. Tumor size was routinely monitored every 3 d by means of a caliper.

Immunizations with IECs isolated from the gut. Donor mice were treated with OXA (10 mg per kg) i.p. for 6 h to induce IEC death. Control animals were treated with vehicle (PBS) alone. The composition of the commensal gut microbiota in the treated and nontreated groups was maintained and synchronized by cohousing. At 6 h post-OXA (or PBS), mice were killed and the ileum and/or colon were collected to isolate IECs. One million IECs from ilea or colons were then injected s.c. into the left flank of recipient naive mice. The procedure was repeated once, 7 d later. Tumor challenge was performed on the right flank 7 d after the last immunization with MTD, doses which obtain 100% of tumor incidence in naive mice, that is MC38 (1 × 10^6 cells), MCA205 (0.8 × 10^6 cells), CT26 (1 × 10^6 cells) and 4T1 (0.3 × 10^6 cells). In indicated experiments, IECs were pretreated with 100 mM PPADS (Sigma), 200 µM DNP (Sigma) or vehicle for 20 min at 4 °C. Treated cells were washed three times with cold PBS before injection or IECs were co-injected with neutralizing anti-HMGB1 Ab (ab18256, Abcam), anti-calreticulin Ab (NB600-101, Novus Biologicals) or rabbit IgG isotype control (NBP2-24891, Novus Biologicals) at 10 µg per injection.

In indicated experiments, T cell depletion was performed by i.p. injections of anti-CD4 (clone GK1.5, 200 µg per mouse), anti-CD8 mAbs (clone 53-6.72; 200 µg per mouse), anti-CXCL13 (clone 143614R, 500 µg per mouse, from R&D) anti-IL12p40 (clone C17.8; 500 µg per mouse), anti-IL12p70 (clone R2-9A5; 500 µg per mouse) or respective isotype controls (LTF-2, 2A3, rat IgG2a, rat IgG2b). Depletion treatment started 1 d before first vaccination and was repeated at the same dose for the second vaccination. B cell depletion was performed as previously described[53]. Briefly, mice were injected i.p. with the following mixture of monoclonal Abs at 150 µg per mouse each: rat anti-mouse CD19 (clone 1D3), rat anti-mouse B220 (clone RA3-6B2, from BioLegend) and mouse anti-mouse CD22 (clone CY34). After 48 h, the mice were injected with a secondary Ab mouse anti-rat κ immunoglobulin light chain (clone MAR 18.5) at 150 g per mouse (all Abs from BioXCell, unless otherwise indicated).

Immunizations with IECs from ileum-derived organoids. Organoids were treated with 10 µg ml^{-1} OXA for 3 h. In indicated experiments, IECs were admixed with pasteurized ileal mucus collected from patient samples as adjuvants and were then injected s.c. (10^6 IEC cells and 50 µl of mucosal material at 500 mg ml^{-1}) into

the left flank of the recipient mice. The procedure was repeated once, 7 d later. Tumor challenge was performed on the right flank 7 d after the last immunization. *Alistipes onderdonkii*, *Erysipelatoclostridium ramosum*, *Bacteroides uniformis* and *Streptococcus gallolyticus* isolates were isolated in our laboratory from ileal mucosal material from patients used in vaccination experiments. In the indicated experiments, organoids were treated with 10 µg ml^{-1} OXA for 3 h in the presence of 10^6 pasteurized bacteria per milliliter.

Immunotherapy. Mice were treated i.p. with anti-PD-1 (250 µg per mouse; clone RMP1-14, BioXcell) or the appropriate isotype control (clone 2A3) at 4 d after OXA (or PBS) treatment. Four total injections every 3 d were performed.

Gut dissociation to collect IECs. Ilea and/or colons were collected and fat tissue, Peyer's patches and feces were removed. Intestines were cut longitudinally and then cut transversally into small pieces into a tube. Pieces were transferred into a new 50-ml tube with 20 ml of IEC medium (PBS, 5% FCS, 5 mM EDTA and 1 mM DTT), vortexed and shaken at 37 °C for 15 min. Cell suspensions were collected in a new tube, filtered with a cell strainer (100 µm), centrifuged, resuspended in PBS and stored on ice until use. In indicated experiments villi and crypt cells were isolated as previously described[54]. Briefly, pieces of ileum were washed in cold PBS and villi cells were recovered by mechanical isolation, by means of repetitive pipetting. This procedure was repeated until limpid supernatant was obtained. The remaining ileal tissue was incubated in crypt chelating buffer (IEC medium) to recovered crypt cells as described above.

Organoid cultures. Crypts were isolated and enriched from the ileum of 8–12-week-old C57BL/6J mice as previously described[54] with the following modifications. Briefly, washed pieces of ileum were incubated in crypt chelating buffer (2 mM EDTA in PBS) for 30 min on ice. Following the removal of crypt chelating buffer, fragments were vigorously rinsed three times with PBS containing 10% FCS and filtered through a 70-µm cell strainer (BD Bioscience). Crypts were pelleted, washed with Advanced DMEM/F12 (Invitrogen), resuspended in 1 ml of Matrigel growth factor reduced basement membrane matrix (Corning) and 50-µl drops were pipetted into a 24-well plate. Crypts were overlaid with Advanced DMEM/F12 containing the following: 100 U ml^{-1} penicillin G sodium, 100 µg ml^{-1} streptomycin sulfate, 2 mM L-glutamine, 10 mM HEPES, 1× N2 supplement, 1× B27 supplement, 50 ng ml^{-1} mEGF, 100 ng ml^{-1} mNoggin (Peprotech), *N*-acetylcysteine (Sigma) (reagents from Invitrogen unless otherwise indicated) and 10% conditioned medium of R-Spondin-1 transfected HEK 293 T cells.

FMT experiments. Frozen fecal samples collected from proximal colon were thawed and thoroughly vortexed. Large particulate material was allowed to settle by gravity. Then, 200 µl of supernatant was administered in a single dose by oral gavage into GF mice. Additionally, an extra 100 µl was topically applied onto the fur of each animal. The resulting gnotobiotic mice were maintained in positive-pressurized isolators with irradiated food and autoclaved water. Two weeks after FMT, tumor cells were injected s.c. and mice were treated with OXA or vehicle (PBS) as described above. Baseline colonization was assessed by 16S rRNA sequencing of fecal gene amplicons within each group of mice before starting any treatment (refer to Supplementary Fig. 2). Immunotherapy. SPF mice were treated with ATB cocktail for 3 d (to sterilize the gut) that was discontinued 24 h before performing the oral gavage with the patient sample. After 2 weeks, tumor was inoculated and bacterial gavage, OXA and anti-PD-1 injections performed as described for the SPF model.

Gut colonization with dedicated commensal species. We used several converging biological and/or clinical readouts to classify bacteria that fell into each of the two immunogenic versus tolerogenic categories as follows: (1) in vitro assays using Flt3-derived DC: no/low IL-12 associated with tolerogenic bacteria; (2) in vivo experiments using i.p. OXA + oral gavages of bacteria: no raise in serum IgG/IgG2b responses, no increase of T_{FH} cells in tdLNs but instead, accumulation of T_H17 cells in tdLNs associated with tolerogenic bacteria; (3) in vivo experiments using FMT following by therapeutic OXA + oral gavages or vaccination with organoids ± bacteria: no control of MC38 tumor growth associated with tolerogenic bacteria; and (4) correlative studies between 16S rRNA sequencing of ileal gene amplicons and PFS in the whole cohort of patients with pCC: no significant impact on PFS associated with tolerogenic bacteria.

Species tested were isolated from samples for this study by culturomics. Species were grown on Columbia agar with 5% sheep blood plates in aerobic or an anaerobic atmosphere created using anaerobic generators (Biomerieux) at 37 °C for 24–72 h. Colonization of SPF, GF or avatar (FMT) mice was performed by oral gavage with 100 µl of suspension containing 10^9 bacteria in PBS. For bacterial gavage, suspensions of 10^9 c.f.u. ml^{-1} were obtained using a fluorescence spectrophotometer (Eppendorf) at an optical density of 1 measured at a wavelength of 600 nm. Two bacterial gavages were performed for each mouse, the first at 24 h before treatment with OXA and then 24 h after the treatment. The efficacy of colonization was confirmed by qPCR performed on fecal DNA with specific primers for bacterial species (see below) or culturing feces 48 h after the first gavage (Supplementary Fig. 6).

Bacteria identification by qPCR. Total genomic DNA from fecal pellets was extracted with QIAamp Fast DNA Stool Mini Kit (Qiagen) following manufacturer's protocol. Genomic DNA was analyzed by real-time PCR using the Universal Master Mix II (Invitrogen) or PowerUp SYBR Green Master Mix (Invitrogen) according to the manufacturer's instructions using the 7500 Fast Real-Time PCR system or Quant Studio 3 (Applied Biosystems). Expression was normalized to the expression of the total bacterial load determined by Universal 16S RNA gene by means of the $2^{-\Delta Ct}$ method. All primers were from Thermo Fisher Scientific (Supplementary Table 6).

Characterization of mLN immune gene expression profile by RT–qPCR. Total RNA from mLNs was extracted with RNeasy Mini Kit (Qiagen) and then reverse transcribed into complementary DNA with SuperScript III reverse transcriptase and RNaseOUT recombinant ribonuclease inhibitor (Life Technologies), in the presence of random primers (Promega) and the deoxynucleoside triphosphate set, PCR grade (Roche Diagnostics). Complementary DNA was analyzed by RT–qPCR with the TaqMan method with TaqMan gene expression assays using the Universal Master Mix II (Invitrogen) according to the manufacturer's instructions, using the 7500 Fast Real-Time PCR system (Applied Biosystems). Expression was normalized to the expression of the housekeeping gene *Ppia* by means of the $2^{-\Delta Ct}$ method. All primers were from the TaqMan gene expression assay (Thermo Fisher Scientific). Mouse primers used were *Ppia* (Mm02342430_g1); *Il12a* (Mm00434165_m1); *Il12b* (Mm00434174_m1); *Il2* (Mm00434256_m1); *Il4* (Mm00445259_m1); *Il6* (Mm00446190_m1); *Il21* (Mm00517640_m1); *Tgfb1* (Mm01178820_m1); *Il1b* (Mm00434228_m1); *Il1a* (Mm00439620_m1); *Tnf* (Mm00443258_m1); *Il10* (Mm01288386_m1); *Il23a* (Mm00518984_m1); and *Ifng* (Mm01168134_m1).

ELISA. For quantification of lipocalin-2 from feces, samples were resuspended (at 100 mg ml^{-1}) in PBS containing 0.5% Tween 20 and incubated with shaking for 20 min at 37 °C. Samples were then centrifuged for 10 min at 12,000 r.p.m. Supernatants were collected and stored at −20 °C until analysis. Lipocalin-2 levels were measured using the Duoset murine Lcn-2 ELISA kit (R&D Systems) following the manufacturer's instructions. For quantification of serum immunoglobulins, sera were collected and stored at −20 °C until analysis. Ig levels were measured using the IgG (total) and IgG2b mouse uncoated ELISA Kits (Thermo Fisher Scientific) following the manufacturer's instructions.

Flow cytometry analyses. The tdLNs were collected at the end of the experiment for the FMT model. The mLNs were collected 7 d post-OXA treatment for gut immunology analysis. Lymph nodes were crushed in RPMI medium or for DC subset analysis, digested with Collagenase D (Worthington) and DNase I (Roche) for 30 min at 37 °C, as previously described[55]. Subsequently, cells were meshed through a 100-µm cell strainer to retrieve single-cell suspensions. In the next step, erythrocytes were lysed by incubation in ACK lysis buffer and filtered through a 40-µm cell strainer. IEC suspensions were obtained from ileum-derived organoids by means of a three-wash dissociation method, as described above. In all cases, 2–10 million cells were pre-incubated with purified anti-mouse CD16/CD32 (clone 93; eBioscience or clone 2.4G2) for 20 min at 4 °C, before membrane staining. For intracellular staining, the Foxp3 staining kit (eBioscience) was used and dead cells were excluded using the Live/Dead Fixable Yellow dead cell stain kit (Life Technologies). For extracellular staining, DAPI was used to exclude dead cells. Anti-mouse Abs (and clones) used for phenotyping were purchased from eBiosciences, BD and BioLegend as follows: CD3e (145-2C11 and 17A2), CD4 (GK1.5 or RM4-5), CD8a (53-6.7), CD11b (M1/70), CD11c (HL3), CD19 (1D3), CD45 (30-F11), CD45R/B220 (RA3-6B2), CD103 (2E7), CD161b/c (PK136), CD172a (P84), CD317 (927), FOXP3 (FJK-16s), CXCR3 (FAB1685P), CX3CR1 (SA011F11), CCR6 (140706), CCR9 (W-1.2), Ly-6C (HK1.4), PD-1 (29F1A12), ICOS (11-9942-82), CXCR5 (2G8), MHC-II/I-A/I-E (M5/114.15.2), Siglec-H (551), TNF-α (MP6-XT22), XCR1 (ZET) and CALR (Polyclonal). Streptavidin PE, annexin V-APC, 7AAD, DAPI and propidium iodide were obtained from BD Pharmingen. Samples were acquired on a Cyan ADP 9-color cytometer (Beckman Coulter), 13-color Cytoflex (Beckman Coulter) or 18-color LSR Fortessa SORP (BD) and analyses were performed with FlowJo software (Tree Star).

Intestinal Ki67 staining and evaluation. OXA was injected i.p. at a dose of 10 mg per kg. Mice were killed 72 h later and small and large intestines were collected and fixed with formalin for subsequent immunohistochemistry. FFPE sections from the small and large intestine were deparaffinized and rehydrated through a series of graded alcohols and distilled water. Antigen retrieval was performed by pre-treating sections with citrate buffer (pH 6.0, DAKO REAL) for 20 min in a microwave (700 W) and then for 30 min at room temperature. Endogenous peroxidase activity was inhibited by treating sections with 3% hydrogen peroxidase for 30 min. Sections were blocked with 1× Teng-T for 30 min at room temperature. The primary polyclonal rabbit Ab, Ki67 (NCL ki67p, Novocastra, 1:1,000 dilution) was incubated overnight, followed by the secondary Ab, biotinylated anti-rabbit (BA-1000, Vector) for 1 h. Peroxidases were detected with di-amino-benzidine-peroxidase substrate kit (Vectastain Elite, PK6100, Vector) and counterstained with Mayer's hematoxylin and Alcian blue.

Immunohistochemistry staining and analysis of cleaved caspase-3 expression. Composition and cellularity were assessed using H&E. The 3-µm-thick sections of FFPE ileum and colon from treated and untreated mice were mounted on poly-L-lysine-coated slides, deparaffinized and rehydrated through a series of graded alcohols and distilled water. Antigen retrieval was performed by pre-treating sections with 0.01 M sodium citrate buffer (pH 6.0, Diapath) for 30 min in a 98 °C water bath. Endogenous peroxidase activity was inhibited by treating sections with 3% hydrogen peroxidase (S202386, DAKO) for 10 min. Sections were blocked with IHC/ISH Super Blocking Solution (PV6122, LeicaBiosystem) for 10 min. The primary polyclonal rabbit Ab, cleaved caspase-3 (Asp175) (9661, Cell Signalling, dilution 1:100) was incubated for 1 h, followed by the secondary Ab, PowerVision Poly-HRP anti-Rabbit IHC Detection Systems (PV6114, LeicaBiosystem) for 20 min. Peroxidases were detected with diaminobenzidine-peroxidase substrate kit (DAKO), and counterstained with Mayer's hematoxylin. Images displayed in the figures were acquired as whole-slide images (WSIs) with a slide scanner Olympus VS120 at ×20 objective. For detecting murine crypts, a deep-learning-based method was used. Briefly, pathologists trained a neural network to perform semantic segmentation of villi, crypts, lamina propria and muscle in murine ileum and colon. WSIs were cropped into 256 × 256 pixels tiles. Blank tiles and tiles with only debris or uninterpretable pieces of tissue were excluded by pathologists. Cropped tiles were processed by the neural network-based semantic segmentation model and crypt images were obtained. QuPath software was used to detect DAB-positive cells[56] and the cell density of positive cCasp3 cells in crypts was calculated.

Immunohistochemistry staining, scanning and analysis of double-staining BCL6-CD4. Mouse anti-human BCL6 monoclonal Ab (DAKO, M7211, clone PG-B6p, 20 µg ml^{-1}) and rabbit anti-human CD4 monoclonal Ab (Spring, clone SP35) were performed on 3-µm-thick sections of FFPE ileum, colon and adenocarcinoma of colon from the same patients with a Benchmarck Ultra automated immunostainer (Ventana, Gustave Roussy Cancer Campus). Antigen retrieval was performed by incubating slides in CC1 buffer (EDTA, pH 8.0) for 92 min at 95 °C. Then BCL6 Ab was incubated for 80 min at room temperature and CD4 Ab for 1 h at 37 °C. Abs were detected by respectively Amplification OptiView kit (Roche, 760-099) and OptiView DAB (Roche, 760-700) and Amplification kit (Roche, 760-080) and UltraView RED (Roche, 760-501). Finally, the sections were counterstained by hematoxylin I (Roche, 760-2021) and bluing reagent (Roche 760-2037). Images for analysis were acquired as WSIs with a slide scanner Zeiss Axio Scan.Z1 and Olympus VS120. To classify and quantify BCL6 and/or CD4$^+$ cells, QuPath software was used[56]. Regions of interest (ROIs) were defined first by the 'Simple Tissue Detection' function and modified by hand in each WSI. After detecting all cells in ROIs, QuPath was interactively trained to classify CD4$^-$BCL6$^+$ cells using morphology and intensity measurements of all detected cells. CD4$^+$BCL6$^+$ cells were quantified manually. Cell density was calculated by dividing the total number of cells in each population by area of ROIs.

Immunohistochemistry staining and analysis of IL-1β in murine ileum and colon. Composition and cellularity were assessed using H&E. Then, 3-µm-thick sections of FFPE ileum and colon from mice were mounted on poly-L-lysine-coated slides, deparaffinized and rehydrated through a series of graded alcohols and distilled water. Antigen retrieval was performed by pre-treating sections with 0.01 M sodium citrate buffer (pH 6.0, Diapath) for 30 min in a water bath at 98 °C . Endogenous peroxidase activity was inhibited by treating sections with 3% hydrogen peroxidase (S202386, DAKO) for 10 min. Sections were blocked with IHC/ISH Super Blocking Solution (PV6122, LeicaBiosystem) for 10 min. The primary monoclonal mouse Ab, IL-1b (3A6) (12242 S, Cell Signalling, dilution 1:50) was incubated for 1 h, followed by the mouse Ab enhancer and secondary Ab, Klear Mouse HRP-Polymer DAB Detection System (D52-18, Golden Bridge International) for 15 min, respectively. Peroxidases were detected with DAB Plus Substrate System (TA060HDX, Thermo Fisher Scientific), and counterstained with Mayer's hematoxylin. Images displayed in the figures were acquired as WSIs with a slide scanner Olympus VS120 at ×20 objective. For mouse tissue analysis, QuPath software was used[56]. ROIs were defined firstly by 'Simple Tissue Detection' function and modified by hand in each WSI. DAB-positive cells within the ROIs were quantified and the cell density of positive IL-1b cells was calculated.

Intestinal toxicity analysis. For histological analysis, longitudinal sections were counterstained with H&E. For histological quantitative analysis, inflammatory foci, appearance of the submucosa, length of villi and the thickness of lamina propria were scored for each section by a pathologist (P.O.). The score was defined as: 0, normal, 0+, focal and minor lesions; 1, diffuse and minor lesions; 2, diffuse, minor and major lesions; and 3, major lesions with areas containing only connective tissue.

Culturomics analyses. The bacterial diversity of the ileal mucus samples used for the vaccination experiments was explored using a culturomics approach[57,58]. Each sample was inoculated in aerobic and anaerobic blood culture bottles. Tenfold serial dilutions of the liquid cultures were subsequently plated on 5% sheep blood enriched Columbia agar (BioMerieux) and incubated respectively in aerobic conditions for 48 h and in anaerobic conditions for 1 week. Obtained colonies were subcultured and routinely identified using a matrix-assisted laster desorption ionization time-of-flight mass spectrometer (Microflex, Bruker Daltonics)[59]. In case of a failed routine identification, the colony was identified by sequencing the 16S rRNA gene. For each bacterial taxon, a mean frequency was calculated in two groups defined according to the response to the vaccination. A relative frequency difference was calculated for each species to determine which species were enriched or depleted. Statistical significance of the relative frequency difference was determined using uncorrected chi-squared test, comparing the proportion of each taxon in the two groups.

16S rRNA gene sequencing. Characterization of metagenomic communities was performed through amplification and sequencing of hyper-variable regions.

For human samples, genomic DNA extraction, library preparation and sequencing were conducted at GATC Biotech AG. Amplification was performed using region-specific primers that target conserved regions flanking the variable regions, V3–V5. Sequencing was performed with Illumina MiSeq technology.

For mouse samples, total genomic DNA from fecal pellets was extracted with QIAamp Fast DNA Stool Mini Kit (Qiagen) following the manufacturer's protocol. Sequencing of obtained DNA was performed at IHU Méditerranée Infection, targeting the V3–V4 regions of the 16S rRNA gene with Illumina MiSeq technology.

Microbiota characterization. Raw FASTQ files were analyzed with Mothur pipeline v.1.39.5 for quality check and filtering (sequencing errors, chimerae) on a Workstation DELL T7910 (Round Rock). Raw reads (213,457,810 in total, on average 652,776 per sample) were filtered and clustered into operational taxonomical units (OTUs), followed by elimination of low-populated OTUs (after five reads), downsampling (the real rarefaction step) of each sample to the number of reads present in the less-populated sample and by de novo OTU picking at 97% pair-wise identity using standardized parameters and SILVA rDNA Database v.1.19 for alignment. In all, 1,001 OTUs were identified. Sample coverage was computed with Mothur and was on average equal to 99% for all samples (mean ± s.e.m., 99.4% ± 0.5%), thus indicating a suitable normalization procedure for subsequent analyses. Analysis of similarity (which represents the difference of datasets' centroids) with 999 permutations or, when requested, Spearman correlation coefficient, were computed with SciKit-Bio package v.0.4.1. Linear discriminant analysis effect size analysis was employed on the relative abundances of bacterial species that were statistically different after Mann–Whitney *U*-test (for pair-wise comparison) or Kruskal–Wallis test (for multiple comparison). Benjamini–Hochberg two-stage false detection rate (FDR) at 10% was then applied, with the additional constraint in leaving only the species that were represented by at least five datapoints.

OTU species assignment and multivariate statistical analyses. Bioinformatic and statistical analyses on recognized OTUs were performed with Python v.2.7.11. The most representative and abundant read within each OTU (as evidenced in the previous step with Mothur v.1.39.5) underwent a nucleotide Blast using the National Center for Biotechnology Information (NCBI) Blast software (ncbi-blast-2.3.0) and the latest NCBI 16S Microbial Database (ftp://ftp.ncbi.nlm.nih.gov/blast/db/). We used an optimized workflow encompassing both SILVA database alignment/classification and NCBI BLAST with the highest Evalue and percentage identity. This approach allowed us to resolve difficult genera such as *Bacteroides* at the species level. A matrix of bacterial relative abundances was built at each taxon level (phylum, class, order, family, genus and species) for subsequent multivariate statistical analyses. Raw matrix (tabular) data were first normalized, then standardized using QuantileTransformer and StandardScaler methods from SciKit learn package v.0.20.3. Normalization using the output_distribution = 'normal' option transforms each variable to a strictly Gaussian-shaped distribution, while the standardization results in each normalized variable have a mean of zero and variance of one. These two steps of normalization followed by standardization ensure the proper comparison of variables with different dynamic ranges, such as bacterial relative abundances. Measurements of α diversity (within-sample diversity) such as observed_otus and Simpson index, were calculated at the OTU level using the SciKit learn package v.0.4.1. Exploratory analysis of β diversity (between-sample diversity) was calculated using the Bray–Curtis measure of dissimilarity calculated with Mothur and represented in principal-coordinate analyses, whereas for hierarchical clusterization analysis, 'Bray–Curtis' metrics and a 'complete linkage' method were used, implementing in-house scripts (Python v.2.7.11). To compare microbiota taxa with gene expression datasets, a multivariate statistical Spearman correlation analysis (and related *P* values) was performed with in-house Python scripts. Mann–Whitney *U*-test and Kruskal–Wallis tests were employed to assess significance for pair-wise or multiple comparisons, respectively, taking a *P* value ≤0.05 as significant after Benjamini–Hochberg two-stage FDR at 10%.

Statistical analysis. Data analyses and representations were performed either with the statistical environment R (http://www.R-project.org/), Microsoft Excel or Prism 6 (GraphPad). Tumor growth in mouse models was analyzed with dedicated software (https://kroemerlab.shinyapps.io/TumGrowth)[60]. Briefly, data

were subjected to a linear mixed-effect modeling applied to log pre-processed tumor surfaces. *P* values were calculated by jointly testing whether both tumor growth slopes and intercepts (on a log scale) were different between treatment groups of interests. In FMT experiments, comparisons between the efficacy of OXA for each FMT are derived from the estimated slope between treatments, contrasting OXA-PBS for each FMT-treated mouse. Contrasts were transformed to be interpreted as percentage improvement of the tumor size per day of treatment. The Mann–Whitney *U*-test was used to compare two independent groups, whereas nonparametric Kruskal–Wallis tests were implemented for multiple groups. For comparisons between patient groups, the Mann–Whitney *U*-test *P* value was used. A chi-squared test was used for categorical variables to test differences in proportions between groups. Survival curves were estimated using the Kaplan–Meier product limit method. Cox models were estimated with PFS and overall survival as outcomes on the basis of each gene or cell measurement value. All tests were two-tailed and *P* values <0.05 were considered to be statistically significant.

Reporting Summary. Further information on research design is available in the Nature Inquiry Reporting Summary linked to this article.

Data availability

All raw sequencing data and de-aggregated and de-identified patient and mouse metadata can be found at the NCBI Sequence Read Archive (https://www.ncbi.nlm.nih.gov/bioproject or https://www.ncbi.nlm.nih.gov/sra/) under accession number PRJNA478491 (Ileal Apoptosis and Microbiome Shape Immunosurveillance and Prognosis of Proximal Colon Cancer).
All BioSample (PATIENTS_Metadata.csv, MICE_Metadata.csv) and Run Metadata files (PATIENTS_Run.csv, MICE_Run.csv) are also provided in Supplementary Dataset 1 to ease metadata availability.

References

47. Rizvi, S. et al. YAP-associated chromosomal instability and cholangiocarcinoma in mice. *Oncotarget* **9**, 5892–5905 (2018).
48. Barker, N. et al. Identification of stem cells in small intestine and colon by marker gene Lgr5. *Nature* **449**, 1003–1007 (2007).
49. Förster, R. et al. A putative chemokine receptor, BLR1, directs B cell migration to defined lymphoid organs and specific anatomic compartments of the spleen. *Cell* **87**, 1037–1047 (1996).
50. Hildner, K. et al. Batf3 deficiency reveals a critical role for $CD8a^+$ dendritic cells in cytotoxic T cell. *Immunity* **322**, 5 (2008).
51. Rodríguez, C. I. et al. High-efficiency deleter mice show that FLPe is an alternative to Cre-loxP. *Nat. Genet.* **25**, 139–140 (2000).
52. Madison, B. B. et al. Cis elements of the villin gene control expression in restricted domains of the vertical (crypt) and horizontal (duodenum, cecum) axes of the intestine. *J. Biol. Chem.* **277**, 33275–33283 (2002).
53. Keren, Z. et al. B cell depletion reactivates B lymphopoiesis in the BM and rejuvenates the B lineage in aging. *Blood* **117**, 3104–3112 (2011).
54. Sato, T. et al. Single Lgr5 stem cells build crypt-villus structures in vitro without a mesenchymal niche. *Nature* **459**, 262–265 (2009).
55. Lehmann, C. H. K. et al. DC subset-specific induction of T cell responses upon antigen uptake via Fcγ receptors in vivo. *J. Exp. Med.* **214**, 1509–1528 (2017).
56. Bankhead, P. et al. QuPath: open source software for digital pathology image analysis. *Sci. Rep.* **7**, 16878 (2017).
57. Lagier, J.-C. et al. The rebirth of culture in microbiology through the example of culturomics to study human gut microbiota. *Clin. Microbiol. Rev.* **28**, 237–264 (2015).
58. Lagier, J.-C. et al. Culture of previously uncultured members of the human gut microbiota by culturomics. *Nat. Microbiol.* **1**, 16203 (2016).
59. Seng, P. et al. Ongoing revolution in bacteriology: routine identification of bacteria by matrix-assisted laser desorption ionization time-of-flight mass spectrometry. *Clin. Infect. Dis.* **49**, 543–551 (2009).
60. Enot, D. P., Vacchelli, E., Jacquelot, N., Zitvogel, L. & Kroemer, G. TumGrowth: an open access web tool for the statistical analysis of tumor growth curves. *Oncoimmunology* **7**, e1462431 (2018).

Acknowledgements

We thank the animal facility team at Gustave Roussy. We thank technicians and pathologists from Centre GF Leclerc: L. Guyard, L. Arnould and S. Ladoire. We thank S. Brutin, A. Paci, M. Vétizou, T. Yamazaki, J.-E. Fahrner and A. G. Goubet for technical assistance. We thank D. Goere, R. Bonnet, P. Sauvanet, D. Pezet, J. Gagnière, F. Pagani and A. Martinetti for helping with human samples collection. We thank M. Merad, for scientific advice. We thank R. Förster (Institut für Immunologie) and J. A. Harker (Imperial College) for providing knockout models. L.Z. and G.K. were supported by the Ligue Contre le Cancer (Equipe Labelisée); Agence Nationale de la Recherche (ANR) Francogermanique ANR-19-CE15-0029, ANR Projets blancs; ANR under the frame of E-Rare-2, the ERA-Net for Research on Rare Diseases; Association pour la Recherche sur le Cancer; BMS Foundation, Cancéropôle Ile-de-France; Chancelerie des Universités de Paris (Legs Poix), Fondation pour la Recherche Médicale; a donation by Elior; the European Commission (ArtForce); the European Research Council; Fondation Carrefour; Institut National du Cancer; Inserm; Institut Universitaire de France; LeDucq Foundation; the LabEx Immuno-Oncology; the RHU Torino Lumière (ANR-16-RHUS-0008); H2020 ONCOBIOME, the Seerave Foundation; the SIRIC Stratified Oncology Cell DNA Repair and Tumor Immune Elimination; the SIRIC Cancer Research and Personalized Medicine (CARPEM); FHU CARE, Dassault and Badinter Philantropia and the Paris Alliance of Cancer Research Institutes. D.D. was supported by the German Research Foundation (CRC1181-A7). B. Ryffel was supported by Centre National de la Recherche Scientifique, the University of Orleans, the Conseil Général du Loiret and European Regional Development Fund (FEDER No. 2016-00110366 and EX005756). M.C. was supported by ITMO Cancer AVIESAN (Alliance Nationale pour les Sciences de la Vie et de la Santé, National Alliance for Life Sciences & Health) within the framework of the Cancer Plan (HTE201601).

Author contributions

The authors responsible for conceptualization were M.P.R. and L.Z. The authors responsible for performing experiments and data collection were M.P.R., S.Y., C.P.M.D., M.P., G.F., M.T.A., C. Rauber, C.H.K.L., B. Routy, S. Becharef, P. Ly, E.P., C.F., R.D., A.F., A.V., S.K., P.O., F.M. and P.D. The authors responsible for formal data analysis were C. Richard, L.D., C.K., P. Lepage and V.I. The author responsible for data curation was V.I. The authors responsible for reagents, animal models and clinical sample resources were D.D., I.V.S., M.C., S. Benoist, J.-Y.S., A.H., D.M., F. Pietrantonio, F. Pagès, I.G.B., A.E., D.R., F.G., B. Ryffel and P.V. The author responsible for methodology and creation of models was T.V.B. The authors responsible for writing of the original draft were M.P.R. and L.Z. The authors responsible for writing (review and editing) were M.P.R., G.K. and L.Z. The author responsible for visualization was M.P.R. The authors responsible for supervision were G.K. and L.Z. The authors responsible for funding acquisition were G.K. and L.Z.

Competing interests

L.Z. and G.K. are cofounders of EverImmune, a biotech company devoted to the use of commensal bacteria for the treatment of cancers.

Additional information

Extended data is available for this paper at https://doi.org/10.1038/s41591-020-0882-8.

Supplementary information is available for this paper at https://doi.org/10.1038/s41591-020-0882-8.

Correspondence and requests for materials should be addressed to L.Z.

Peer review information Saheli Sadanand was the primary editor on this article and managed its editorial process and peer review in collaboration with the rest of the editorial team.

Reprints and permissions information is available at www.nature.com/reprints.

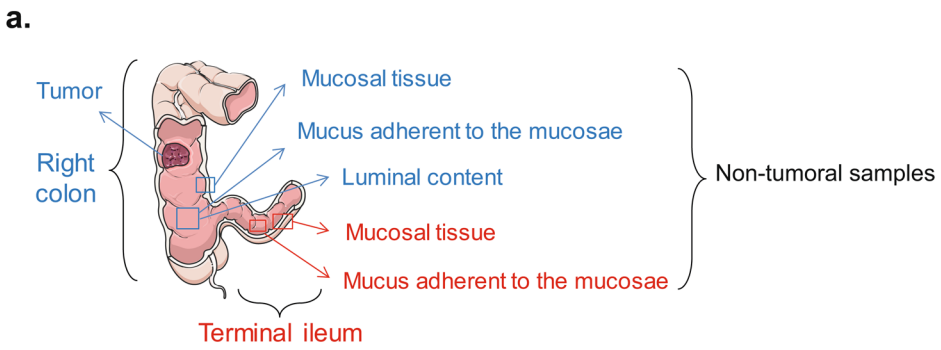

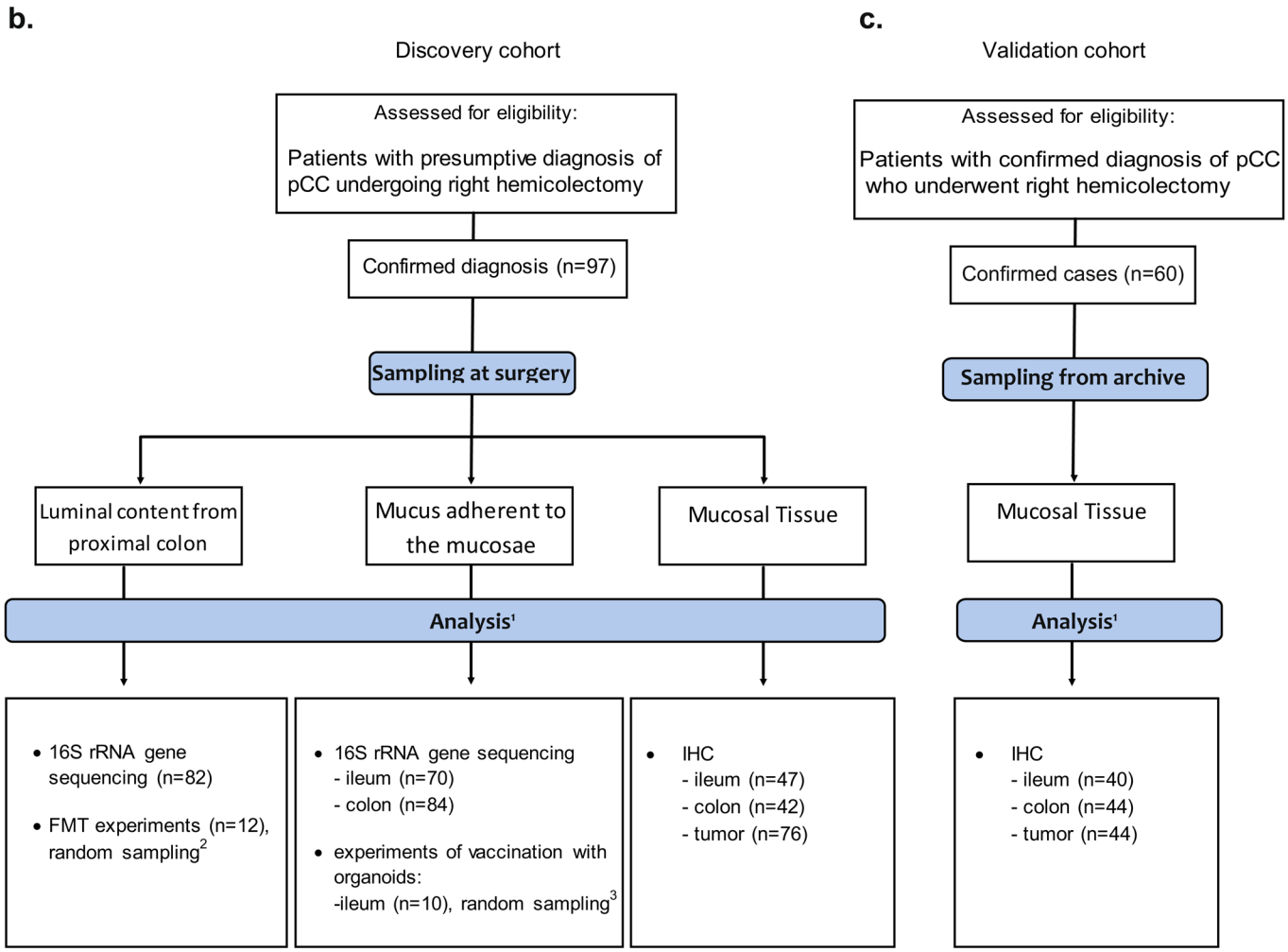

[1]The difference between confirmed diagnosis cases and the analyzed samples corresponds to missing or excluded samples that did not meet the quality control criteria.
[2]Refer to Supplementary table 4 for individual sample details.
[3]Refer to Supplementary table 5 for individual sample details.

Extended Data Fig. 1 | Description of sample origin and pCC cohorts. a, Schematic view of the anatomic distribution of the specimen utilized in the clinical study. Ileal and colonic materials and sampling from patients that have been utilized for various analyses are described. **b-c**, Enumeration of samples for each type of experiments or analyses in both cohorts.

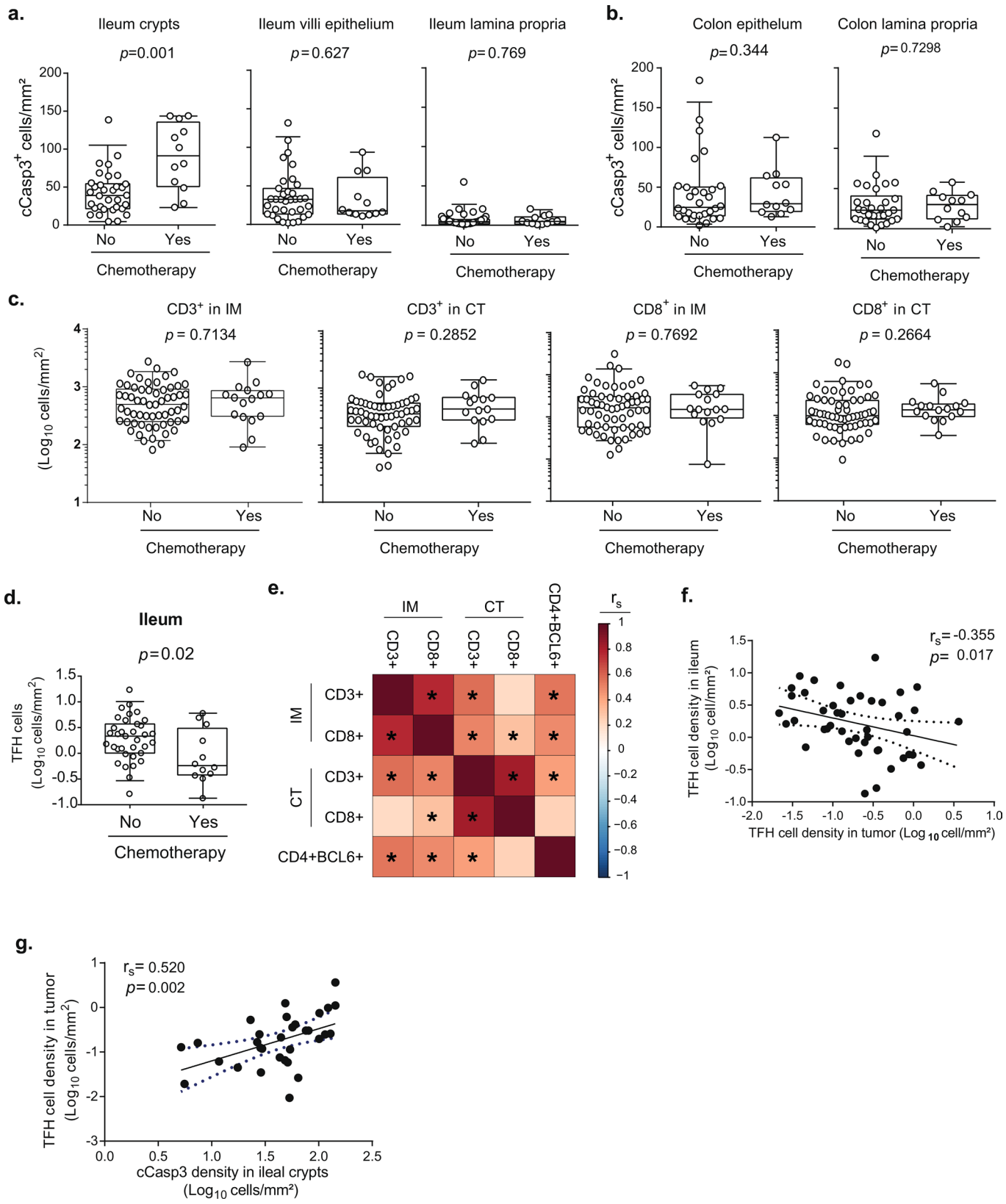

Extended Data Fig. 2 | See next page for caption.

Extended Data Fig. 2 | Ileal apoptosis and microbiome dictate prognosis in stage IV proximal colon cancer. a-**b**, Automated quantification of cleaved in immunohistochemical staining of paired ilea (**a**) and colons (**b**) in different tissue compartments (lamina propria, villus, crypts) of pCC patients from the discovery cohort (Supplementary Table 1), with preoperative chemotherapy or untreated prior to surgery. Non-previous chemotherapy ileum n = 35, colon n = 30; previous chemotherapy ileum n = 12, colon n = 12.Each dot represents one pCC patient, box plot center lines correspond to the median value; lower and upper hinges correspond to the first and third quartiles (the 25th and 75th percentiles); and lower and upper whiskers extend from the box to 5 and 95 percentiles, respectively. Two-tailed Mann Whitney U test p-value is shown. **c**, Quantification of T lymphocytes in tumor beds (according to the immunoscore methodology, CD3 and CD8, in IM (invasive margin) and CT (core of tumor)) in the discovery cohort of pCC patients, with preoperative chemotherapy or untreated prior to surgery. Non-previous chemotherapy: $CD3^{-}$IM n = 59, CD3-CT n = 59, CD8-IM = 60, CD8-CT = 60; previous chemotherapy CD3-IM n = 16, CD3-CT n = 15, CD8-IM = 16, CD8-CT = 16. Each dot represents one pCC patient, Box plot center lines correspond to the median value; lower and upper hinges correspond to the first and third quartiles (the 25th and 75th percentiles); and lower and upper whiskers extend from the box to 5 and 95 percentiles, respectively. Two-tailed Mann Whitney U test p-value is shown. **d**, Quantification of TFH in the lamina propria of pCC patients with available data from discovery cohort. Non-previous chemotherapy n = 35; previous chemotherapy n = 12. Each dot represents one pCC patient, boxes and whiskers depict medians, first and third quartiles and ± 5^{-}95 percentiles, respectively. Two-tailed Mann Whitney U test p-value is shown. **e**, Heatmap of correlations between immunoscore components shown in (**c**) and TFH ($CD4^{+}Bcl6^{+}$) for n = 40 patients with available data in the discovery cohort. Spearman's rank coefficients of correlation (rs) and two-tailed *p*-values<0.05 (*) are depicted. **f**, Correlation between TFH densities in ileum and tumor paired samples from pCC patients of the discovery cohort. Each dot represents one pCC patient, n = 44. The continuous and dotted lines show the regression line and 95% of confidence intervals, respectively. Spearman's rank coefficient of correlation (rs) and two-tailed p-value are shown. **g**, Correlation between the number of ileum crypt cells positive for cleaved caspase 3 stainings and TFH cell density in tumors from stage IV patients from the discovery and validation cohort, n = 31. The continuous and dotted lines show the regression line and 95% of confidence intervals, respectively. Spearman's rank coefficient of correlation (rs) and two-tailed *p*-value are shown.

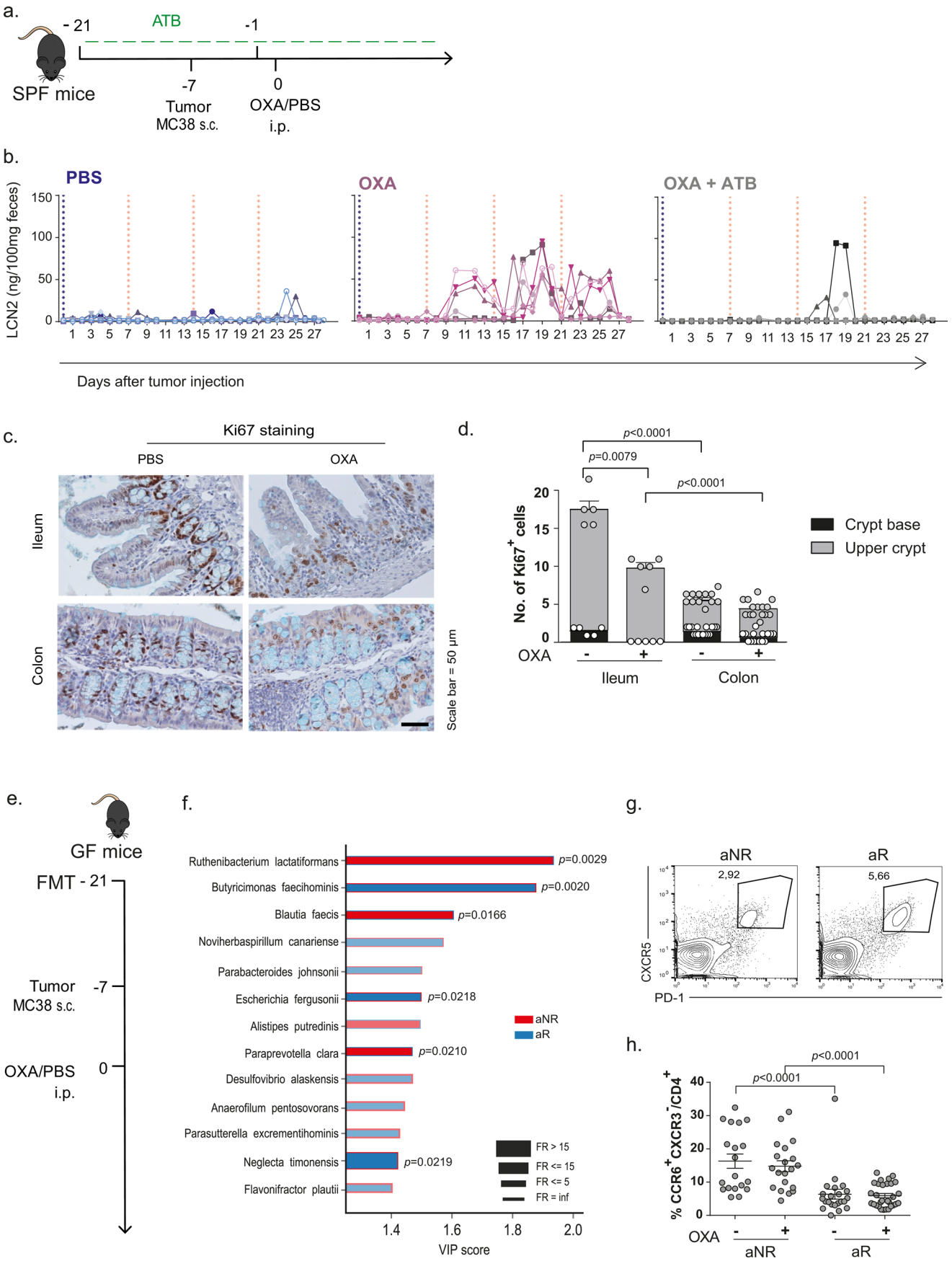

Extended Data Fig. 3 | See next page for caption.

Extended Data Fig. 3 | Impact of the microbiome in the efficacy of OXA in MC38 tumor bearers. a, Experimental setting (**a**) for Fig. 2a and S2b. ATB were administered for 2 weeks prior to s.c. injection of MC38. OXA was administered on day 7 without ATB interruption. **b**, Lipocalin-2 (LCN2) levels in a kinetics study monitored by ELISA in stools of tumor bearing mice treated with OXA (or PBS) i.p. ± ATB treatment. Blue dotted lines indicate day of tumor s.c. injection and orange dotted lines indicate day of OXA/PBS treatments. n = 5 mice/group. **c**, Representative micrographs of immunohistochemical staining for Ki67 in ileal and colonic mucosae 3 days after i.p. OXA (or PBS) treatment in WT mice. One experiment. **d**, Quantification of $Ki67^+$ cells in ileal (PBS n = 5, OXA n = 5) and colonic (PBS n = 14, OXA n = 15) crypts and according to cellular compartment. Each dot represents one sample, mean ± SEM is depicted. **e**, Experimental setting for Fig. 2d. FMT was performed in germ-free mice 2 weeks prior to s.c. injection of MC38. OXA (or PBS) is administered i.p. on day 7. Mice are housed in isolators throughout the experiment. **f**, The PLS-DA / VIP method was used to compare abundances of all bacterial species between aNR (n = 35) and aR (n = 72) subgroups. Species with differential abundance between both groups were used as input for the Partial Least Square Discriminant Analysis to calculate the variable importance (VIP score > 1). Two-stages Benjamini-Hochberg False Detection Rate (FDR) at 10% was applied on normalized and standardized relative abundances before PLS-DA / VIP analysis. **g**, Representative flow cytometry plots of TFH cells in tdLN 21 days post PBS or OXA treatment in tumor bearers in aR versus aNR. Staining for PD-1, and CXCR5 in $CD4^+$ T cells gated on the viable $CD3^+CD45^+$ population. $CXCR5^{hi}PD\text{-}1^{hi}$ cells within live $CD4^+$ T cells from one representative aNR and one aR mouse treated with OXA are shown. In total, 4 aNR and 4 aR groups were evaluated; concatenated data of all individual samples is shown in Fig. 2g. **h**, FACS determination of $CCR6^+CXCR3^-/CD4^+$ T cells gated in the viable $CD3^+CD45^+$ population in tumor tdLN in aR and aNR mice with or without OXA treatment on day 21 at sacrifice. Concatenated data from 12 FMT patients. Each dot represents one mouse, mean ± SEM is depicted. aNR PBS n = 19, aNR OXA n = 20; aR PBS n = 22, aR OXA n = 30. Refers to Fig. 2f. Statistics: Mann-Whitney U test used to compare two independent groups (after Kruskal-Wallis was implemented for multiple groups) (**d**, **f**, **h**). Significant two-tailed *p*-values are shown in the figures.

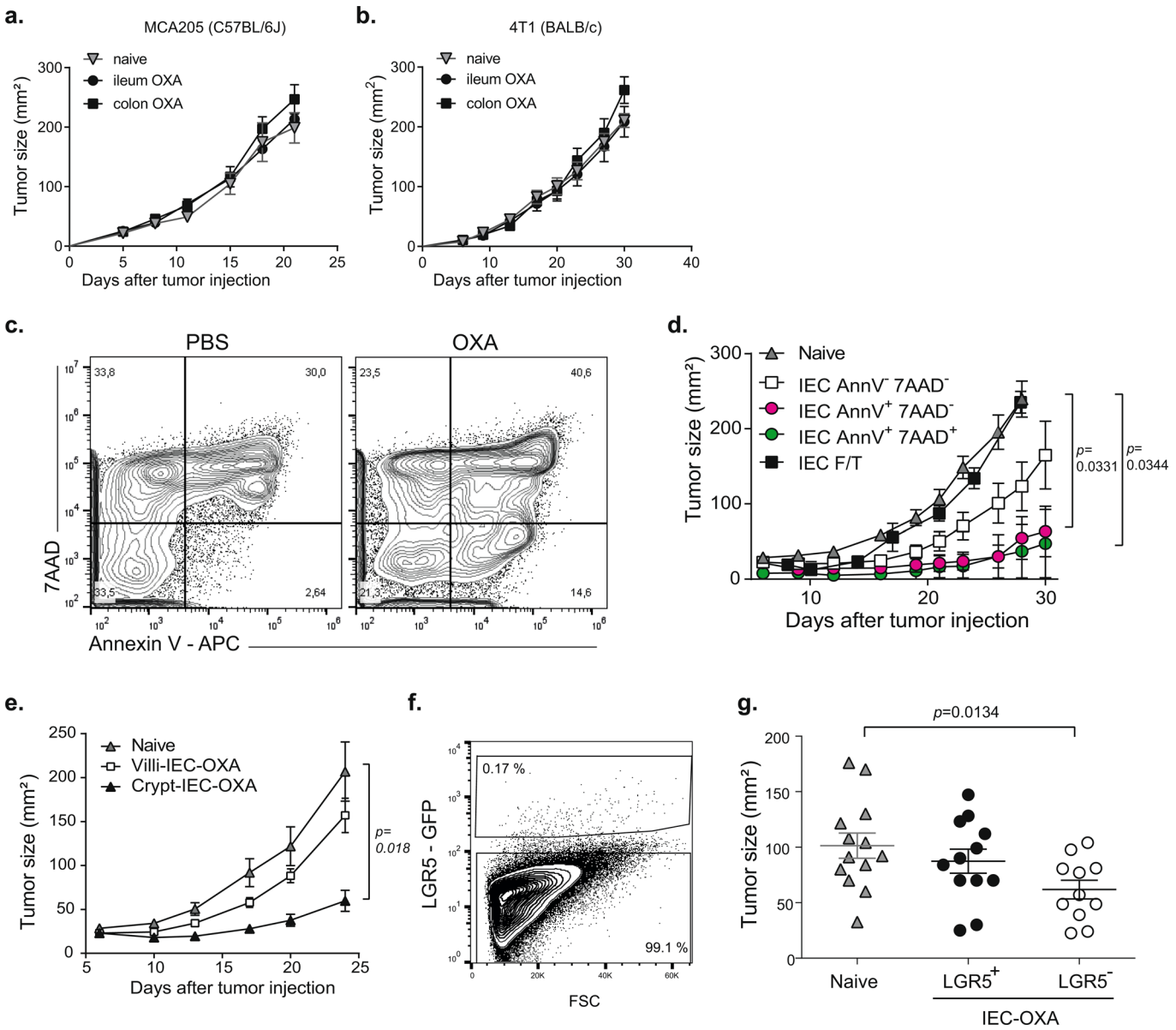

Extended Data Fig. 4 | Protective role of intestinal caspases -3 and -7 in the cell death of ileal IEC against colon cancer. a-**b**, Vaccination of naïve C57BL/6 J (**a**) or BALB/c (**b**) mice using ileal or colonic IEC which were exposed to OXA to protect against syngeneic transplantable colon cancers (such as MC38 or CT26, respectively (Fig. 3a-b)) or irrelevant syngeneic tumors (such as MCA205 (**a**) and 4T1 (**b**), respectively. Tumor growth curves showing one representative experiment out of 3 yielding similar results. MCA205 n = 5/group. 4T1 naïve n = 6, ileum-OXA n = 6, colon OXA n = 5. Mean ± SEM is depicted. **c**-**d**, Dying ileal IEC were harvested at 6 h post-OXA i.p. and separated by a FACS cell sorting based on Annexin V/7AAD expression or vaccination with IEC subjected to three freeze-thaw cycles (F/T) before being inoculated as a vaccine in naive mice as described in Fig. 3a. A representative flow cytometric analysis is shown (**c**) and tumor growth kinetics of MC38 in recipients vaccinated with the four cell subsets are depicted (**d**). Naïve n = 6, IEC annV-7AAD- n = 5, IEC annV+7AAD- n = 5, IECAnnV+7AAD + n = 6, IEC F/T n = 10. Mean ± SEM is depicted. **e**, Vaccination as in Fig. 3a but using an IEC cell suspension enriched in villi versus crypt cells. Naïve n = 5, Villi IEC OXA n = 10, Crypt IEC OXA n = 10. Mean ± SEM is depicted. **f**, Representative FACS dot plot of the IEC fraction from Lgr5⁻EGFP-IRES-creERT2 mice used for lineage-tracing of Lgr5-expressing stem cells of the small intestine. One representative sorting data out of two performed. **g**, Id. as in Fig. 3a but vaccination has been performed using ileal IEC composed of either LGR5⁺ (purity > 95%) or LGR5⁻. Tumor size at day 21 in 2 pooled experiments is shown, each dot representing one mouse. Naïve n = 13, LGR5⁺ n = 12, LGR5⁻ n = 11. Means ± SEM are represented. Statistics: mixed-effect modeling with a specific software (Methods) for longitudinal tumor growth analysis (**a**, **b**, **d**, **e**) and Mann-Whitney U test used to compare two independent groups (after Kruskal-Wallis was implemented for multiple groups) (**g**). Significant two-tailed *p*-values are shown in the figures.

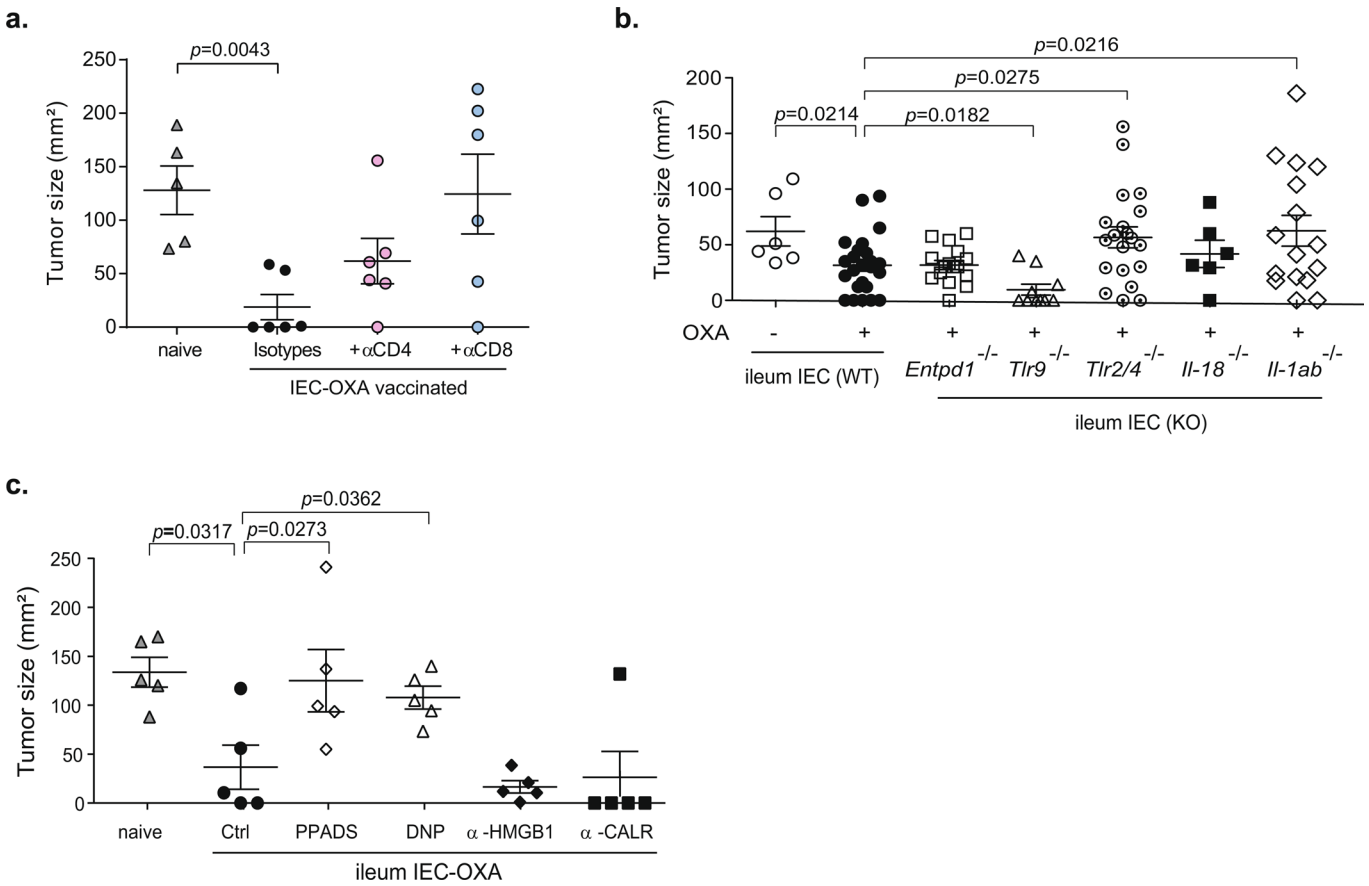

Extended Data Fig. 5 | Immunogenic cell death of ileal IEC. a, Dying (OXA-exposed) ileal IEC were administered two weeks apart as in Fig. 3a. in WT C57BL/6 mice cotreated with CD4 or CD8 T cell depleting Abs or their isotype control Abs. CD4 and CD8 levels in peripheral blood were monitored and after their full recovery to baseline levels, mice were challenged with the MTD of MC38. Tumor sizes at sacrifice are depicted in a representative experiment. Naïve n = 5, Isotypes n = 6, αCD4 n = 6, αCD8 n = 6. **b**, MC38 tumor sizes at sacrifice in mice vaccinated with OXA-exposed ileal IEC harvested in mice harboring different genotypes WT (PBS n = 6, OXA n = 24) versus *Cd39/Entpd1*$^{-/-}$ (n = 16), *Tlr9*$^{-/-}$ (n = 10), *Tlr2/4*$^{-/-}$ (n = 20), and *Il1a/b*$^{-/-}$ (n = 6) and *Il18*$^{-/-}$ (n = 16). Pooled data from 3 independent experiments, mean ± SEM is depicted. **c**, Ileal IECs from OXA-treated mice were injected into wild type C57BL/6 J mice, along with the ATP-depleting agent dinitrophenol (DNP) and the purinergic P2Y2 receptor antagonist pyridoxalphosphate-6-azophenyl-2',4'-disulphonic acid (PPADS) or neutralizing antibodies anti-HMGB1 or calreticulin before to challenging of recipient mice with the MTD of MC38. Tumor sizes at sacrifice are indicated. A representative experiment out of two is shown, comprising n = 6 mice/group, mean ± SEM is depicted. Statistics: Mann-Whitney U test used to compare two independent groups (after Kruskal-Wallis was implemented for multiple groups). Significant two-tailed *p*-values compared to vaccination controls are shown in the figures.

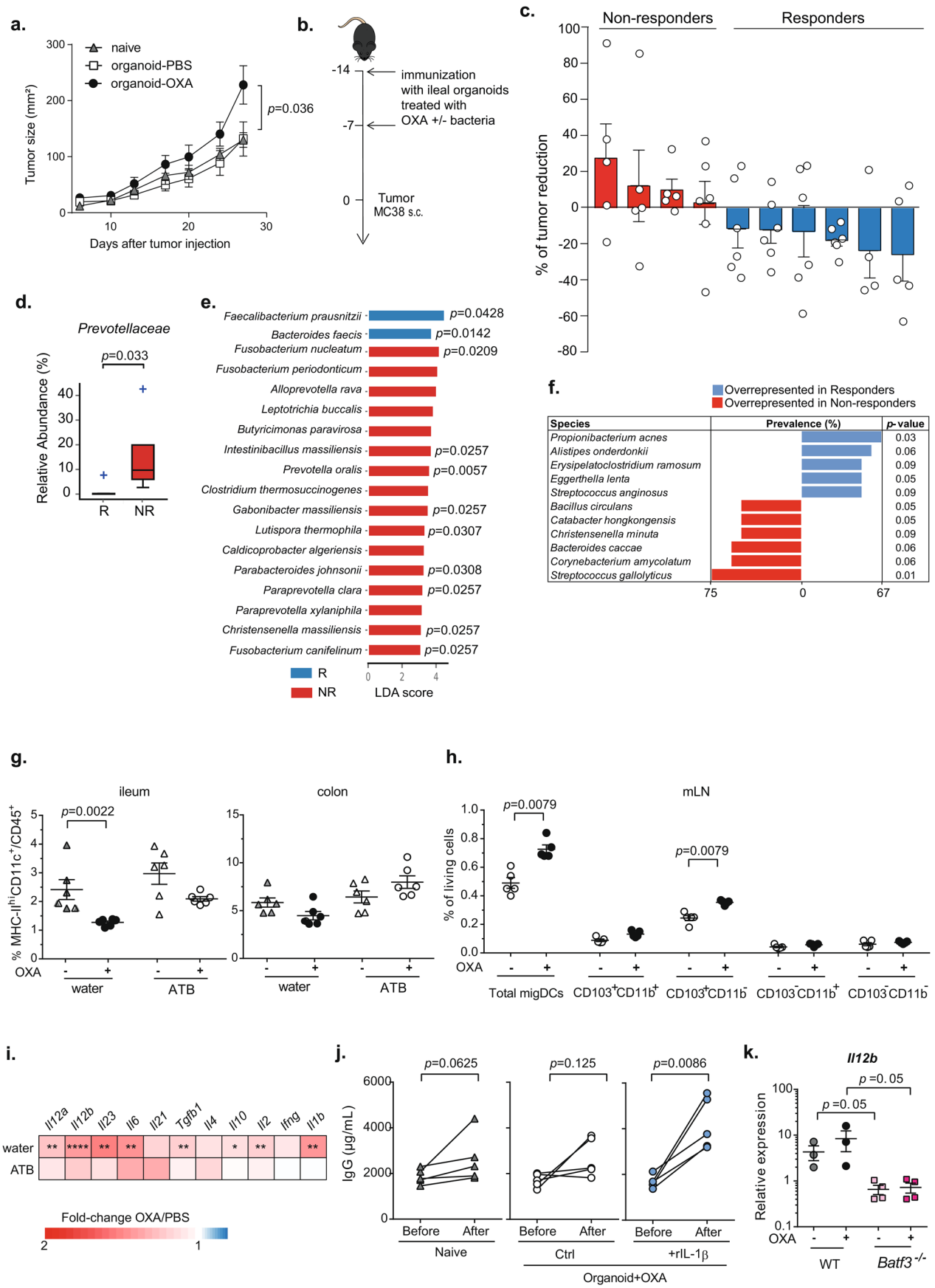

Extended Data Fig. 6 | See next page for caption.

Extended Data Fig. 6 | Role of the ileal microbiome in the adjuvanticity of ileal cell death. a, Tumor growth kinetics of MC38 after vaccination with OXA-exposed ileal stem cell -derived enteroids to immunize WT hosts. Naïve n = 5, organoid-PBS n = 6, organoid-OXA n = 5. Mean ± SEM is depicted. **b**, Experimental setting aimed at reverting tolerance into immunogenicity using ileal organoids: Ileal stem cell derived organoids from WT C57BL/6 J mice were or were not exposed to one of ten pCC patients' mucosal ileal microbiota and OXA ex vivo prior to s.c. injection to immunize naive mice against MC38. Details of each donor patient in Supplementary Table 5. Controls included organoids exposed to OXA alone, or ileal microbiota alone (without organoids. **c**, Percentages of tumor size reduction between immunized and naive mice at day 21 segregating responders (R) from non-responders (NR) based on statistical analyses on tumor growth kinetics. Sample sizes from left to right n = 5, 5, 5, 6, 6, 6, 6, 6, 4, 5. Mean ± SEM is depicted. **d**, Comparison between R (n = 6) and NR (n = 4) at family taxonomic rank level. Relative abundance of *Prevotellaceae* family. Box plot center lines correspond to the median value; lower and upper hinges correspond to the first and third quartiles (the 25th and 75th percentiles). **e**, Linear discriminant analysis (LDA) coupled with the effect size measurements to represent species differentially present among R (n = 6) and NR (n = 4). LEfSe plots were generated with Python 2.7 and all species with LDA score ≥ 2 are shown. *p*-values show significant differences in pair-wise analyses between NR and R. **f**, Culturomics-based determination of the bacterial species from ileal mucosa microbiota. Significant differences in detection of distinct bacterial species between R and NR performed in the 10 PCC patients. Chi-square test p-values are shown. **g**-**h**, Flow cytometric analyses of migratory dendritic cells, cDC1 and cDC2 in lamina propria of ilea or colons (**g**, n = 6/group) or mLN (h, n = 5/group) in mice treated with OXA +/- ATB. One representative experiment out of two yielding similar results. Mean ± SEM is depicted. **i**, Heatmap representation of RT-PCR based- relative ratios of immune gene transcripts in mLN at 24 h post-OXA i.p. vs PBS with or without ATB. Water groups n = 11, ATB groups n = 5. **j**, Humoral immune responses monitored by ELISA (IgG) after 4 weeks of vaccination using OXA- exposed ileal organoids compensated or not with rIL-1β (n = 6/group, one representative experiment out of 2 yielding similar results). Two-sided Wilcoxon signed-rank test. **k**, Il12b gene product in WT versus *Batf3* KO mice. WT groups n = 3, *Batf3*$^{-/-}$ groups n = 4. Mean ± SEM is depicted. Statistics: unless otherwise specified, mixed-effect modeling with a specific software (Methods) for longitudinal tumor growth analysis (**a**) and Mann-Whitney U test used to compare two independent groups (after Kruskal-Wallis was implemented for multiple groups) (**d**, **e**, **g**, **h**, **k**). Significant two-tailed *p*-values are shown in the figures; for (**i**): $^{*}p < 0.05$, $^{**}p < 0.01$, $^{***}p < 0.001$, $^{****}p < 0.0001$.

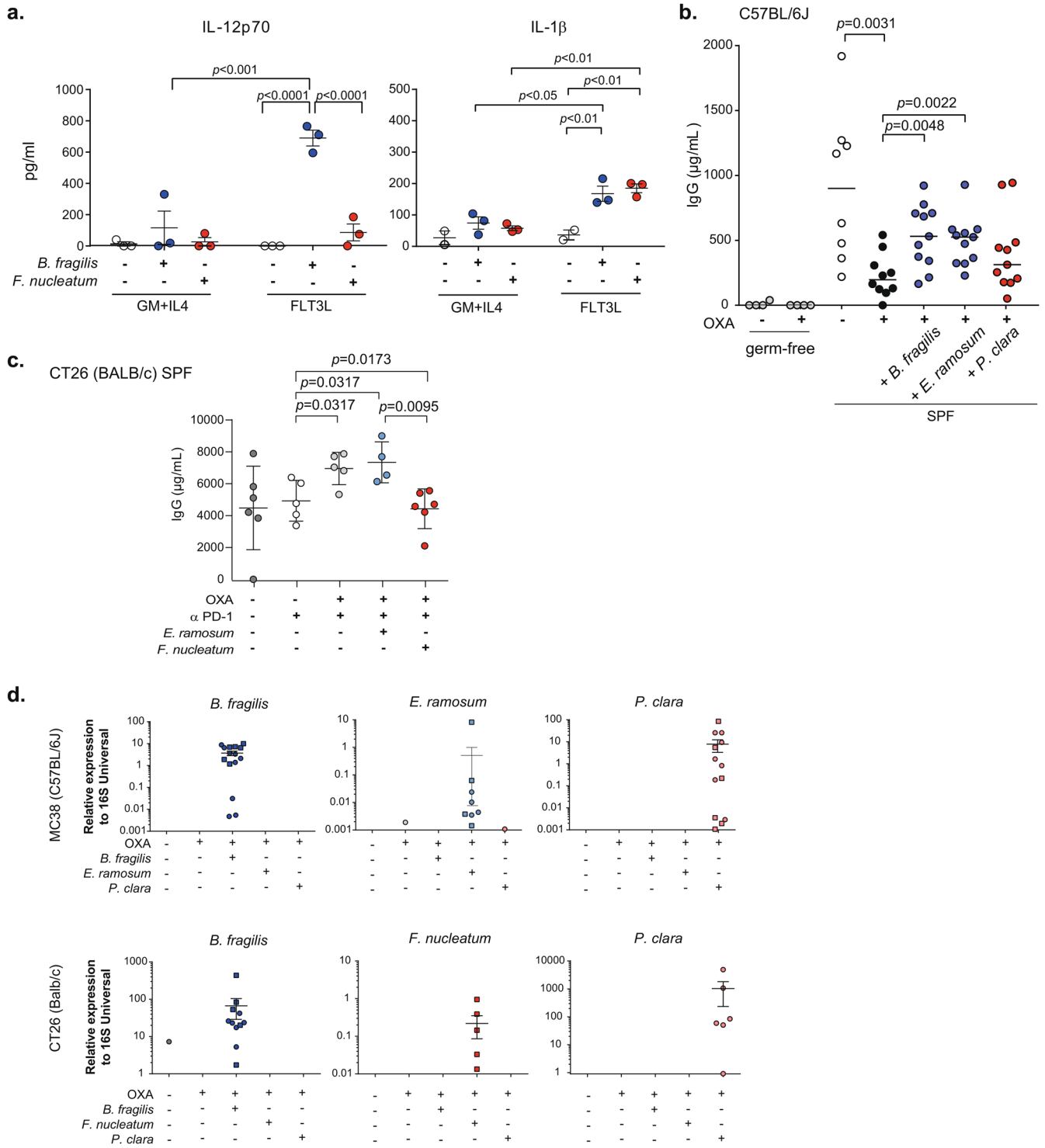

Extended Data Fig. 7 | Immunogenic ileal commensals induce DC IL-12 and IL-1β release and IgG humoral immune responses. a, ELISA monitoring of cytokine release (IL-1β, IL-12p70) by BM-derived DC cultured in GM-CSF + IL-4 or FLT3L conditions (which differentiate into cDC1) pulsed with various live commensals (for 2 h followed by killing with ATB for 22 h). A representative experiment out of two performed yielding similar results is shown, run in experimental triplicates. Mean ± SEM is depicted. Two-way ANOVA with Bonferroni's correction. Significant two-tailed *p*-values are shown in the figure. **b**, IgG humoral responses evaluated by ELISA in the serum of mice, which were treated with OXA (day 0) and oral gavaged with the indicated commensals at day -1 and +1. Analysis was performed at day 7. Data pooled from two independent experiments. Germ-free groups n = 4, SPF PBS n = 8, SPF OXA n = 10, *B. fragilis* n = 11, *E. ramosum* n = 11, *P. clara* n = 11. Median value is depicted. Mann-Whitney U test. Significant two-tailed *p*-values are shown in the figure. **c**, IgG humoral responses evaluated by ELISA in the serum of mice, in the experimental setting described in Fig. 6f. Mean ± SEM is depicted. Mann-Whitney U test. Significant two-tailed *p*-values are shown in the figure. **d**, Quantitative PCR using dedicated and specific probe sets to monitor colonization of various commensals at day +2 post-first and second oral gavage. Data from two experiments (performed in C57BL/6 J (upper panel) or in BALB/c (lower panels)) are depicted, one dot representing one feces. Detected values by qPCR are shown, mean ± SEM is depicted. Analyzed sample sizes in C57BL/6 J groups: PBS n = 19, OXA n = 17, *B. fragilis* n = 16, *E. ramosum* n = 16, *P. clara* n = 21. Analyzed sample sizes in BALB/c: n = 6/group.

nature research

Corresponding author(s): Laurence Zitvogel

Last updated by author(s): Mar 6, 2019

Reporting Summary

Nature Research wishes to improve the reproducibility of the work that we publish. This form provides structure for consistency and transparency in reporting. For further information on Nature Research policies, see Authors & Referees and the Editorial Policy Checklist.

Statistics

For all statistical analyses, confirm that the following items are present in the figure legend, table legend, main text, or Methods section.

n/a	Confirmed	
☐	☒	The exact sample size (*n*) for each experimental group/condition, given as a discrete number and unit of measurement
☐	☒	A statement on whether measurements were taken from distinct samples or whether the same sample was measured repeatedly
☐	☒	The statistical test(s) used AND whether they are one- or two-sided *Only common tests should be described solely by name; describe more complex techniques in the Methods section.*
☐	☒	A description of all covariates tested
☐	☒	A description of any assumptions or corrections, such as tests of normality and adjustment for multiple comparisons
☐	☒	A full description of the statistical parameters including central tendency (e.g. means) or other basic estimates (e.g. regression coefficient) AND variation (e.g. standard deviation) or associated estimates of uncertainty (e.g. confidence intervals)
☒	☐	For null hypothesis testing, the test statistic (e.g. *F*, *t*, *r*) with confidence intervals, effect sizes, degrees of freedom and *P* value noted *Give P values as exact values whenever suitable.*
☒	☐	For Bayesian analysis, information on the choice of priors and Markov chain Monte Carlo settings
☒	☐	For hierarchical and complex designs, identification of the appropriate level for tests and full reporting of outcomes
☐	☒	Estimates of effect sizes (e.g. Cohen's *d*, Pearson's *r*), indicating how they were calculated

Our web collection on statistics for biologists contains articles on many of the points above.

Software and code

Policy information about availability of computer code

Data collection	For scanning of histological slides: Axio Scan.Z1 (Zeiss, Germany) NanoZoomer HT2.0 (Hamamatsu photonics, Japan) Olympus VS120 (Olympus, Japan) Cyan ADP 9 colors cytometer (Beckman Coulter), 13 color Cytoflex (Beckman Coulter), and 18 color LSR Fortessa SORP (BD). StepOne software and QS3 (Thermofisher). XT Benchmark (Ventana USA).
Data analysis	Visiopharm Integrator System (VIS) (Visiopharm A/S, Denmark) and QuPath (version 0.1.3 and 0.2.0-m8) Segmentation Model (version 0.2.1), Keras (version 2.2.2), Zeiss Zen 2 lite software (Zeiss Germany) Tensorflow (version 1.10.0), and Python (version 3.5.5) FlowJo software Tree Star v10 (Ashland, OR, USA). Microsoft Excel 2016 under Windows 10 Microsoft Co.(Redmont, WA, USA). Prism 6 GraphPad (San Diego, CA, USA). Tumor growth software (Our laboratory, access at https://kroemerlab.shinyapps.io/TumGrowth). Developer XD image analysis software (Definiens, Germany). Mothur v.1.39.5. meta R-package. SciKit-Bio

For manuscripts utilizing custom algorithms or software that are central to the research but not yet described in published literature, software must be made available to editors/reviewers. We strongly encourage code deposition in a community repository (e.g. GitHub). See the Nature Research guidelines for submitting code & software for further information.

Data

Policy information about availability of data

All manuscripts must include a data availability statement. This statement should provide the following information, where applicable:

- Accession codes, unique identifiers, or web links for publicly available datasets
- A list of figures that have associated raw data
- A description of any restrictions on data availability

All raw sequencing data can be found at the NCBI Sequence Read Archive (accession number: PRJNA478491; "Ileal Apoptosis and Microbiome Shape Immunosurveillance and Prognosis of Proximal Colon Cancer", https://www.ncbi.nlm.nih.gov/bioproject/?term=PRJNA478491, or https://www.ncbi.nlm.nih.gov/sra/PRJNA478491).
For both patients (submission ID SUB4218459) and mice (submission ID SUB6655852), raw fastq.gz files and de-aggregated and de-identified metadata are provided at the following SRA Run Selector link:
https://www.ncbi.nlm.nih.gov/Traces/study/?query_key=4&WebEnv=NCID_1_50416433_130.14.22.76_5555_1583484624_2234475021_0MetA0_S_HStore&o=acc_s%3Aa.
All BioSample (PATIENTS_Metadata.csv, MICE_Metadata.csv) and Run Metadata files (PATIENTS_Run.csv, MICE_Run.csv) are also provided as supplementary information to ease metadata availability.

Field-specific reporting

Please select the one below that is the best fit for your research. If you are not sure, read the appropriate sections before making your selection.

☒ Life sciences ☐ Behavioural & social sciences ☐ Ecological, evolutionary & environmental sciences

For a reference copy of the document with all sections, see nature.com/documents/nr-reporting-summary-flat.pdf

Life sciences study design

All studies must disclose on these points even when the disclosure is negative.

Sample size	No sample-size calculation was performed. For human studies, number of samples was selected based on disponibility of the samples. The results obtained in the human cohorts were consistent with those from animal models and prior human studies. Novel results from this study were consistent in both discovery and validation cohorts, as well. For mouse experiments, sample sizes were decided based on previous publications and experience and common standards in similar field, for calculating statistical significance. Experiments were performed with positive/negative controls at the same sample size to verify reliability of results. For all data subjected to statistical analyses, results from two or more independent repeats were used. Sample sizes and number of independent experiments are always indicated in the figure legends.
Data exclusions	All sample exclusions (due to QC or scientific reasons) were performed prior to data analysis. See Extended Data Figure 1 for details.
Replication	The number of replicates for each specific experiment is indicated throughout the manuscript text and figure legends. All attempts of replication were successful.
Randomization	Mice of same age and gender were randomized for all in vivo experiment. Mice were randomly allocated in the different experimental groups, ensuring only an equal distribution tumor sizes for therapeutic experiments.
Blinding	The investigators were blinded to group allocation during data collection and analysis.

Reporting for specific materials, systems and methods

We require information from authors about some types of materials, experimental systems and methods used in many studies. Here, indicate whether each material, system or method listed is relevant to your study. If you are not sure if a list item applies to your research, read the appropriate section before selecting a response.

Materials & experimental systems

n/a	Involved in the study
☐	☒ Antibodies
☐	☒ Eukaryotic cell lines
☒	☐ Palaeontology
☐	☒ Animals and other organisms
☐	☒ Human research participants
☐	☒ Clinical data

Methods

n/a	Involved in the study
☒	☐ ChIP-seq
☐	☒ Flow cytometry
☒	☐ MRI-based neuroimaging

Antibodies

Antibodies used

For in vivo depletion and treatments, the following antibodies are coming from BioXCell : anti-CD4 (cat.ref. : BE0003-1, clone GK1.5 lot : 699918O1), anti-CD8 (cat.ref : BE0004-1, clone 53–6.72 lot : 693018M2), anti-IL12p40 (cat. Ref :BE0051, clone C17.8, lot 717619A1), anti-IL12p70 (cat. ref: BE0233, clone R2-9A5, lot : 670019J3), anti–mouse CD19 (cat.ref : BE0150, clone 1D3, lot : 661017D1), and mouse anti–mouse CD22 (cat. ref : BE0011, clone CY34, lot :599516J1). anti–rat Kappa Immunoglobulin Light Chain (cat. ref. : BE0122, clone MAR 18.5, lot : 697618M1). anti-PD-1 (cat.ref : BE0146, clone RMP1-14, lot : EUX190617).

The following antibody is coming from eBioscience : rat anti–mouse B220 (cat.ref. : 14-0452-86, clone RA36B2, lot: 4338656).
The following antibody is coming from R&D : anti-CXCL13 (cat réf: MAB470, clone 143614R).

Anti-mouse antibodies (and clones) used for FACS phenotyping were purchased :
From eBioscience : CD16/CD32 (cat.ref : 16-0161-86, clone 93, lot : 4344018, dilution 1/400), CD4 (cat.ref. : 11-0042, clone : RM4-5, lot : E00083-213, dilution: 1/400), Foxp3 (cat.ref : 17-5773-82, clone 145-2C11, lot : 8345662, dilution 1/100), ICOS (cat.ref.: 11-9942-82, clone : 7E.17G9, lot : 4315261, dilution 1/100), TNF-α (cat.ref.: 12-7321-82, clone : MP6-XT22, lot: 4318513, dilution 1/100), CD172a (cat.ref : 46-1721-82, clone: P84, lot: 1978151, dilution 1/400), Ly-6C (cat.ref: 47-5932-82, clone: HK1.4, lot: 4346376, dilution 1/800)
From BD : CD3e (cat.ref : 564380, 552774 and 612771, clones: 17A2 and 145-2C11, lot : 8282724, 8345662 and 9197275, dilution : 1/40, 1/100 and 1/400 respectively), CD11c (cat.ref: 562454, clone: HL3, lot: 3261624, dilution : 1/400), CD19 (cat.ref : 612781 and 557655, clone 1D3, lot: 7311608 and 8194765, dilution 1/400 and 1/100), CD45 (cat.ref.: 563053, clone: 30-F11, lot: 4206540, dilution: 1/800), CD161b/c (cat.ref: 564144, clone: PK136, lot: 8250919, dilution 1/400), MHC-II/I-A/I-E (cat.ref: 562366, clone: M5/114.15.2, lot: 7215878, dilution 1/200),
From BioLegend : CD4 (cat.ref: 100531 and 100432, clones : GK1.5, lot : B255834 and B210117, dilution 1/100 and 1/400), CD8a (cat.ref: 100762 and 100740, clone: 53-6.7, lot: B253215 and B229804, dilution 1/100 and 1/400), CD11b (cat.ref: 101222, clone: M1/70, lot: 7180930, dilution 1/400), CD45 (cat.ref.: 103128, clone: 30-F11, lot: B274307, dilution: 1/100), CD45R/B220 (cat.ref: 103210, clone: RA3-6B2, lot: B247904, dilution 1/800), CD103 (cat.ref : 121426, clone 2E7, lot: B236114, dilution 1/800), CD317 (cat.ref: 127019, clone: 927, lot : B242136, dilution 1/400), CX3CR1 (cat.ref : 149031, clone : SA011F11, lot: B253508, dilution 1/400), CCR6 (cat.ref: 564736, clone: 140706, lot: 8344771), CCR9 (cat.ref: 128706, clone: CW-1.2, lot: B211967, dilution 1/100), PD-1 (cat.ref : 135206, clone: 29F.1A12, lot: B265719, dilution 1/800), Siglec-H (cat.ref: 129606, clone: 551, lot: B188521, dilution 1/400), XCR-1 (cat.ref : 148216, clone : ZET, lot: B237775, dilution 1/400)
From BioXCell: CD16/CD32 (cat.ref : BE0008, clone 2.4G2, lot: BX-ER-013, dilution: 1/400)
From Novus Biologicals (Biotechne) : CALR (cat.ref : NB600-101, polyclonal, lot: H-4).
From R&D : CXCR3 (cat.ref: FAB1685P, clone: 220803, lot: LLN0607101)

Validation

All the antibodies used in this study have been validated by the manufacturing companies:
New clone's specificities are tested during product development. In case of any inconsistency, manufacturers do not continue to work with this specific clone.
A same clone and format from former validated lot is always use as reference to further validate a new lot.
Validation is done on a specific organ or sample according to clone and target molecules tested, in parallel with the most relevant control.
Tests are done for every conjugation of antibody (i.e. all availabe formats).

Eukaryotic cell lines

Policy information about cell lines

Cell line source(s)

MC38 cell line was derived from methylcholanthrene-induced murine colon adenocarcinoma cells (NCI, Bethesda, MD). MCA205 cell line derived from methylcholanthrene-induced murine sarcoma was a kindly gift from Mark J. Smith University of Queensland, Australia. 4T1 and CT26 wild-type cancer cell lines were purchased from the American Type Culture Collection (ATCC, Rockefeller, MD, USA). CCA cell line was derived from a syngeniec cholangicarcinoma and was a kind gift from Professor Gregory J. Gores (Mayo Foundation for Medical Education and Research).

Authentication

None of the cell lines have been authenticated

Mycoplasma contamination

All cell lines were tested negative for mycoplasma contamination.

Commonly misidentified lines
(See ICLAC register)

No commonly misidentified cell lines were used.

Animals and other organisms

Policy information about studies involving animals; ARRIVE guidelines recommended for reporting animal research

Laboratory animals

Female C57BL/6J and BALB/c mice were purchased from Harlan (France) and Janvier (France), respectively. Mice were used between 7 and 14 weeks of age.
Mice coming from CDTA (Cryopreservation, Distribution, Typage et Archivage, Orléans, France) :
All mice were C57BL/6J genetic background. Only females were use for germ free experiments. Only males were used for Il1ab-/-, Il18-/- models. Males and females were used for Cd39/Entpd1-/-, Tlr2/4-/- and Tlr9-/- models.
Age and gender of WT littermates for each model were selected to harmonize groups with their KO counterparts.
Lgr5-EGFP-IRES-creERT2 females mice were purchased from The Jackson Laboratory (JAX stock #008875).
Bcl6fl/flCreCD4 mice (males and females) and Bcl6fl/fl littermate controls were a kind gift from Dr. James A. Harker (Imperial

College London, UK).
Homozygous CXCR5-deficient mice (males an females), B6.129S2(Cg)-Cxcr5tm1Lipp/J, and WT littermate controls were a kind gift from Dr. Reinhold Förster (Hannover, Germany).
Batf3-/- mice (males and females) were obtained from the animal facility of University of Erlangen (Germany).
Casp3fl/fl; Casp7fl/fl; Villin-Cre Tg (Caspase3/Caspase7 IEC double KO) (males and females), RIPK3-/-; NntMut/Mut (Rip3k KO) (only females) and respective WT littermate controls (age and gender matched to their KO counterparts) were obtained by Dr. Peter Vandenabeele (VIB-UGent Center for Inflammation Research, Ghent, Belgium).

Wild animals	This study did not involve wild animals.
Field-collected samples	This study did not involve samples collected from the field.
Ethics oversight	All animal experiments were carried out in compliance with French and European laws and regulations. The local institutional board (Ministère de la Recherche, de l'Ensiegnement Supérieur et de l'innovation, MESRI) approved all mouse experiments (permission numbers: 2014-071-1124 and 2017-020-8964). Experiments were performed in accordance with Government and institutional guidelines and regulations (Ministère de la Recherche, de l'Ensiegnement Supérieur et de l'innovation, MESRI).

Note that full information on the approval of the study protocol must also be provided in the manuscript.

Human research participants

Policy information about studies involving human research participants

Population characteristics	The inclusion criteria for the study were patients with right colon adenocarcinoma (at any stage of disease) who underwent right hemi-colectomy plus ileal resection (last 10 centimeters). Patients were over 18 years old and were not on antibiotics at the moment of surgery. See also Supplementary Table 1.
Recruitment	Patients were recruited from Stardard of Care Procedures. Samples and data were collected from 2014 to 2018. No bias was applied. Histological confirmation of colon adenocarcinoma was obtained from pathology reports.
Ethics oversight	Four different health cancer centers participated in the study: Gustave Roussy Cancer Campus (Villejuif, France), Centre G-F Leclerc (Dijon, France) and Hôpital Bicêtre (Le Kremlin-Bicetre, France) in the discovery cohort; Centre G-F Leclerc (Dijon, France) and Istituto Nazionale dei Tumori (Italy) in the validation cohort. Sample collection was conducted according to the ethical guidelines and approval of the local CCPPRB. The study received the legal authorization by the Ministère de l'Enseignement Supérieur et de la Recherche (AC-2013-1884). All participants signed an informed consent to donate the leftovers of their biological samples taken during surgery to the constitution of a biobank for research purposes. Information pertaining to cancer recurrence and death was obtained from hospital records.

Note that full information on the approval of the study protocol must also be provided in the manuscript.

Clinical data

Policy information about clinical studies

All manuscripts should comply with the ICMJE guidelines for publication of clinical research and a completed CONSORT checklist must be included with all submissions.

Clinical trial registration	This study is not a clinical trial.
Study protocol	*Note where the full trial protocol can be accessed OR if not available, explain why.*
Data collection	*Describe the settings and locales of data collection, noting the time periods of recruitment and data collection.*
Outcomes	*Describe how you pre-defined primary and secondary outcome measures and how you assessed these measures.*

Flow Cytometry

Plots

Confirm that:

☒ The axis labels state the marker and fluorochrome used (e.g. CD4-FITC).

☒ The axis scales are clearly visible. Include numbers along axes only for bottom left plot of group (a 'group' is an analysis of identical markers).

☒ All plots are contour plots with outliers or pseudocolor plots.

☒ A numerical value for number of cells or percentage (with statistics) is provided.

Methodology

Sample preparation	Tumor draining lymph nodes (tdLN) were harvested at the end of the experiment for the FMT model. Mesenteric lymph nodes (mLN) were harvested 7 days post-OXA treatment for gut immunology analysis. Lymph nodes were crushed in RPMI medium or, for DC subset analysis, digested with Collagenase D (Worthington) and DNAse I (Roche) for 30 min at 37°C, as previously described54. Subsequently, the cells were meshed through a 100 µm cell strainer to retrieve single cell suspensions. In the next

	step, erythrocytes were lysed by incubation in ACK lysis buffer and filtered through a 40 µm cell strainer. For IEC isolation, ilea and/or colons were collected and fat tissue, Peyer's patches and feces were removed. Intestines were cut longitudinally and then cut transversally into small pieces into a tube. Pieces were transferred into a new 50ml tube with 20ml of IECs medium (PBS, 5% FCS, 5mM EDTA and 1mM DTT), vortexed and shaken at 37°C for 15 min. Cell suspensions were collected in a new tube, filtered with a cell strainer (100µm), centrifuged, resuspended in PBS, and stored on ice until use.
Instrument	CyAn™ ADP Analyzer by Beckman Coulter, CytoFlex by Beckman Coulter, LSR Fortessa SORP by BD.
Software	FlowJo software (Tree Star, Ashland, OR, USA).
Cell population abundance	We obtained a purity of at least 95% of sorted populations determined by Flow cytometry.
Gating strategy	The gating strategy consisted in selecting cells on the size scatter (SS Lin) and forward scatter (FS Lin) followed by an elimination of the doublets based on the size scatter and the pulse width parameters and the removal of dead cells (dead marker positive populations). The downstream gating strategy can be found in figure legends and graph axis.

☐ Tick this box to confirm that a figure exemplifying the gating strategy is provided in the Supplementary Information.